Article

Computation of NMR Shielding Constants for Solids Using an Embedded Cluster Approach with DFT, Double-Hybrid DFT, and MP2

Anneke Dittmer, Georgi L. Stoychev, Dimitrios Maganas, Alexander A. Auer,* and Frank Neese*

Read Online

ACCESS | Metrics & More | Article Recommendations | SI Supporting Information

ABSTRACT: In this work, we explore the accuracy of post-Hartree−Fock (HF) methods and double-hybrid density functional theory (DFT) for the computation of solid-state NMR chemical shifts. We apply an embedded cluster approach and investigate the convergence with cluster size and embedding for a series of inorganic solids with long-range electrostatic interactions. In a systematic study, we discuss the cluster design, the embedding procedure, and basis set convergence using gauge-including atomic orbital (GIAO) NMR calculations at the DFT and MP2 levels of theory. We demonstrate that the accuracy obtained for the prediction of NMR chemical shifts, which can be achieved for molecular systems, can be carried over to solid systems. An appropriate embedded cluster approach allows one to apply methods beyond standard DFT even for systems for which long-range electrostatic effects are important. We find that an embedded cluster should include at least one sphere of explicit neighbors around the nuclei of interest, given that a sufficiently large point charge and boundary effective potential embedding is applied. Using the pcSseg-3 basis set and GIAOs for the computation of nuclear shielding constants, accuracies of 1.6 ppm for ^{7}Li, 1.5 ppm for ^{23}Na, and 5.1 ppm for ^{39}K as well as 9.3 ppm for ^{19}F, 6.5 ppm for ^{35}Cl, 7.4 ppm for ^{79}Br, and 7.5 ppm for ^{25}Mg as well as 3.8 ppm for ^{67}Zn can be achieved with MP2. Comparing various DFT functionals with HF and MP2, we report the superior quality of results for methods that include post-HF correlation like MP2 and double-hybrid DFT.
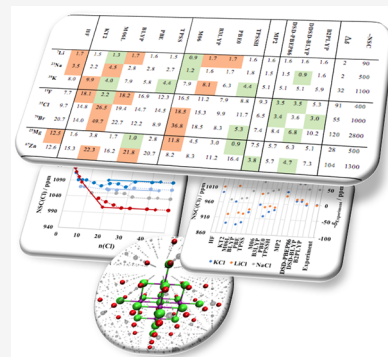
1. INTRODUCTION

Since its introduction,[1,2] nuclear magnetic resonance (NMR) has been established as one of the most widely applied analytical techniques throughout the chemical sciences. Owing to its element-specific and nondestructive nature, as well as its ability to deliver high-resolution spectra, NMR is routinely applied to unravel the local electronic and geometric structure of classes of chemical systems in gas, solution, and solid phases.[3−7]

Interpretation of NMR spectra is routinely based on extracting and analyzing the nuclear magnetic shielding constants, conventionally represented as chemical shifts δ on a relative scale, and the indirect spin−spin coupling constants J. Although it is a common procedure to deduce empirical correlations from tables of experimental spectra, in many cases, safe interpretations are not possible due to the lack of available experimental data, while simple relations are not always reliable. Alternatively, a variety of quantum chemical methods can be employed to compute the NMR nuclear shielding constants (NSCs), helping interpret experimental spectra and connect the indirect structural information contained in measured shifts and spin−spin coupling constants to the electronic structure of the investigated system.[8−10]

For molecular systems, electronic structure methods that are employed to compute NMR NSCs range from Hartree−Fock (HF)[11−13] and density functional theory (DFT)[8,14,15] to post-HF wave-function-based methods like the Møller−Plesset second-order perturbation theory MP2[15−18] and the coupled cluster theory (CC).[19−22] It has been shown that coupled cluster with singles, doubles, and perturbative triples (CCSD-(T)) provides "gold standard" results not only for energies but also for more complex properties like chemical shifts.[23] Although conventional CCSD and CCSD(T) methods can only be applied to small molecules due to the steep scaling of the canonical methods with system size, they have been used to construct reference data sets and evaluate the performances of HF-, DFT-, and MP2-based methods in computing NMR nuclear shielding constants.[15,24,25] These studies have shown that for NMR applications in which a computational approach with predictive power is required, post-HF methods like the CC hierarchy are recommended because they are robust and systematically improvable. MP2 provides the best balance between accuracy and computational cost, performing the best
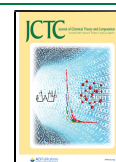
compared against reference CCSD(T) with respect to a variety of common generalized gradient approximation (GGA), meta-GGA, and hybrid DFT functionals.[15,24] A local correlation approach and the resolution of identity approximation RI[26,27] provide access to MP2-level NSC computations for systems with a few hundred atoms, while in combination with linear and sublinear scaling techniques, even larger systems can be treated.[28−30]

Focusing on DFT, it has been demonstrated that the NMR-specialized functionals like KT2[31] have satisfactory performance for computing NSCs although not for their separate dia- and paramagnetic components, due to its flawed description of the density.[32] We have recently shown that NMR NSCs can be efficiently computed by employing double-hybrid functionals in the framework of gauge-including atomic orbitals (GIAOs).[15,33] We have in particular shown that in benchmark calculations the dispersion corrected spin-component-scaled DSD-PBEP86 functional yields chemical shifts with an accuracy superior to MP2.[15]

For solid systems, NMR NSCs are mainly computed at the DFT level of theory in the framework of periodic boundary conditions.[10,34,35] Similar to the GIAO-based molecular methods, the periodic boundary condition methods became widely popular for computing NMR NSCs only after the development of the gauge-including projector augmented wave (GIPAW) scheme.[36] This method extends the original PAW method[36−38] to the computation of NMR shielding constants by restoring the explicit description of the core electrons and additionally minimizing gauge-origin dependence effects using GIAOs. GIPAW NMR NSC calculations are conventionally performed by employing GGA functionals. Hybrid density functionals offer improved accuracy for NMR NSC predictions but at computational costs that are orders of magnitude larger than the respective GGA calculations using plane-wave basis sets, limiting the applicability of the method.[34,38−41]

In recent years, the availability of efficient wave-function-based methods has also allowed one to transfer the accuracy and robustness of post-HF methods not only to large molecular systems but also to problems that traditionally have been treated with periodic boundary DFT methods.[42−44] While plane-wave post-HF methods are currently being developed[45−49] (and Gaussian basis set periodic boundary condition methods have been devised and applied with growing success[50−52]), the strategy of using embedded clusters has witnessed quite some popularity because it provides a conceptually simple path to apply molecular methods to extended systems, provided they fall within the range of applicability of the method.

Conventionally, the embedded cluster models treat the long-range electrostatics and polarization on a molecular mechanics level and can yield results that converge toward the periodic boundary condition limit systematically.[53−59] While embedding strategies have been successfully applied to a broad variety of problems, devising an embedded cluster model for a given system is still a delicate task involving a careful choice of the cluster structure and size, a balanced treatment of the boundary region, and a well-chosen electrostatic environment.[38] For NMR nuclear shielding constants, various cluster approaches have been adopted[38,60−62] to compute solid-state NMR properties, however, up to now, exclusively at the DFT level of theory employing GGA and hybrid density functionals.

In this work, the performance of a variety of bare and embedded cluster computational protocols, performed using MP2 and a variety of DFT methods, will be evaluated for their efficiency and their ability to compute NMR nuclear shielding constants on a benchmark set of inorganic solids.

In particular, it will be shown that by employing carefully designed embedded clusters which allow for large QM regions and very large point charge fields, cluster-size convergence is achieved for the studied systems at all levels of theory. The influence of the employed basis sets on the computed NSCs on bare and embedded clusters is investigated using specialized NMR basis sets and at different levels of theory. In a next step, the best-performing calculation protocol is employed to investigate the performance of MP2 and a variety of DFT methods to compute NSCs across the study set of inorganic solids. For a series of small clusters, DFT and MP2 results will be compared to those of CCSD(T)-computed NSCs. Please note that the NCSs are absolute values as they can be computed via electronic structure methods, while chemical shifts are relative values w.r.t. a standard. In a final step, results obtained using these protocols are compared to experimental chemical shifts and a detailed error analysis is performed. It will be shown that, provided that sufficiently large clusters are employed, the results are insensitive to the chosen embedding scheme such that the residual errors of the calculation are dominated by the residual errors of the methods, namely, the basis set and the level of theory.

2. COMPUTATIONAL DETAILS

All coupled cluster—CCSD and CCSD(T)—calculations were performed using the CFOUR[63] package and pcSseg-n ($n = 1−3$) basis sets, optimized for NMR shieldings.[64] All other nonrelativistic calculations were performed with the ORCA 4.2 suite of programs.[65] NSCs were evaluated at the RI-MP2 and DFT levels of theory using the pcSseg-n ($n = 1−4$) basis sets. A variety of DFT functionals was employed, including the generalized gradient approximation (GGA) functionals KT2,[31] BLYP,[66−68] PBE,[69] and meta-GGAs TPSS[68] and M06L,[66,70] the hybrid functionals M06,[71] B3LYP,[66,67,72] PBE0,[69,73] and TPSSH,[68,74,75] as well as the double-hybrid functionals B2PLYP,[76] DSD-PBEP86,[77,78] and DSD-BLYP.[79] The ORCA calculations were accelerated using the RI approximation for the Coulomb integrals (RI-J),[80] while the exchange terms were computed using the "chain-of-spheres" (COSX) approximation.[81,82] The def2/JK[83] and def2-XVP/C (X = S,T,Q)[84,85] auxiliary basis sets were used for RI-J and RI-MP2, respectively. All NMR DFT computations were performed in the framework of standard, established, uncoupled approximation for DFT.[86−90]

NSCs including relativistic effects and spin−orbit coupling (SOC) on prototype nonembedded systems were computed using the DIRAC19 computational package[91] on the basis of the two-component Barysz−Sadlej−Snijders (BSS)[92−95] Hamiltonian relativistic Kohn−Sham density functional theory that includes noncollinear spin magnetization and involves London atomic orbitals to ensure gauge-origin independent results. The DIRAC calculations were obtained with the PBE0[69,73] functional and the triple-zeta basis set dyall.ae3z.[96,97] These computations capture the essential contribution of the effect of the presence of heavy atoms and also of the NMR chemical shielding constants of adjacent light atoms. To obtain the relativistic corrections, the shieldings were computed with BSS including two-electron spin−orbit corrections by default and with the spin-free[98] version of BSS excluding the spin−orbit corrections, hence only giving the scalar relativistic influence.

The results are compared to the nonrelativistic shieldings computed with the same method by changing the speed of light to 2000 a.u.[99] Further details about the DIRAC calculations can be found in the Supporting Information (SI).

Atomic coordinates of all systems were obtained from the American Mineralogist Crystal Structure Database[100] and the Crystallography Open Database.[101,102] The structures are shown in the Supporting Information in Figure S1.

To treat systems with point charges and ECPs, the necessary contributions were included in the GIAO-NMR implementation in ORCA. Consistent with the notation in ref 32, two terms are added to the Fock matrix

$$F_{\mu\nu} \leftarrow -\sum_{K}^{PCs} q_K \langle \mu | \, |\mathbf{r} - \mathbf{r}_K|^{-1} |\nu\rangle + \sum_{L}^{ECPs} \langle \mu | \hat{V}_L |\nu\rangle \quad (1)$$

The first term, due to the point charges (q_K), is identical to the electron–nucleus interaction term, and its magnetic field derivative presents no additional challenge. The derivative of the second term is discussed by van Wüllen[103] and implemented analogously in ORCA

$$\left. \frac{d\langle \mu_M | \hat{V}_L |\nu_N\rangle}{d\mathbf{B}} \right|_{B=0}$$
$$= \frac{i}{2} \mathbf{O}_{ML} \langle \mu_M | \mathbf{r} \hat{V}_L |\nu_N\rangle - \frac{i}{2} \mathbf{O}_{NL} \langle \mu_M | \hat{V}_L \mathbf{r} |\nu_N\rangle \quad (2a)$$

$$\langle \mu_M | \mathbf{r} \hat{V}_L |\nu_N\rangle = \mathbf{R}_M \langle \mu_M | \hat{V}_L |\nu_N\rangle + \langle \mu_M | \mathbf{r} - \mathbf{R}_M |\nu_N\rangle \nu_N \quad (2b)$$

$$\langle \mu_M | \hat{V}_L \mathbf{r} |\nu_N\rangle = \mathbf{R}_N \langle \mu_M | \hat{V}_L |\nu_N\rangle + \langle \mu_M | \hat{V}_L (\mathbf{r} - \mathbf{R}_N) |\nu_N\rangle \quad (2c)$$

The first terms in eq 2b and c are regular ECP integrals, multiplied by the coordinates of the ECP center, while the second terms require the angular momentum of the bra or ket function to be incremented by one and are also necessary for geometric gradient calculations.

3. BENCHMARK STUDY SET OF SOLIDS

The chosen benchmark set involves solids with a variety of nuclei (halides, chalcogenides, alkali metals, earth alkali metals, and transition metals). Hence, the various bond characters range between highly ionic (e.g., alkali metal halides or MgO) and more covalent (e.g., MgS or ZnS and ZnSe) limits. Also, the set includes elements that are generally regarded as challenging in computational chemistry, such as fluorine. It includes representative examples from the rock salt ($Fm\bar{3}m$) and zinc blende ($F\bar{4}3m$) XY-type structural groups, where X is an element belonging to the metal (Li, Na, K, Mg, Zn) and Y is a halide/chalcogenide (F, Cl, Br, O, S, Se). This includes LiBr, LiCl, LiF, NaBr, NaCl, NaF, KBr, KCl, KF, MgO, and MgS from the rock salt group as well as ZnS and ZnSe from the zinc blende group. The local coordination environment around the X and Y counterparts of the rock salt and zinc blende solids is octahedral (O_h) and tetrahedral (T_d), respectively. For the series, the electrostatic embedding is especially important and the charges in the local environment will have a large effect on the computed property since the electrostatic interaction with neighboring unit cells in a crystal has a significant influence and is typically modeled periodically in contrast to, e.g., molecular crystals.

For all chosen solids, accurate structural data and NMR chemical shifts based on MAS NMR measurements

Table 1. List of Benchmark Sets with Experimental Chemical Shift Values δ

| system	space group	local environment	exp. shift metal δ/ppm	exp. shift halide/chalcogenide δ/ppm
LiBr	rock salt ($Fm\bar{3}m$)	O_h	−2.04 vs LiCl(aq)[85]	64.74 vs KBr(s)[85]
LiCl	rock salt ($Fm\bar{3}m$)	O_h	−1.19 vs LiCl(aq)[85]	1.31 vs KCl(s)[85]
LiF	rock salt ($Fm\bar{3}m$)	O_h	−0.30 vs LiCl(aq)[85]	−74.00 vs KF(s)[85]
NaBr	rock salt ($Fm\bar{3}m$)	O_h	5.04 vs NaCl(aq)[85]	−52.89 vs KBr(s)[85]
NaCl	rock salt ($Fm\bar{3}m$)	O_h	7.21 vs NaCl(aq)[85]	−49.73 vs KCl(s)[85]
NaF	rock salt ($Fm\bar{3}m$)	O_h	7.13 vs NaCl(aq)[85]	−91.00 vs KF(s)[85]
KBr	rock salt ($Fm\bar{3}m$)	O_h	55.10 vs KCl(aq)[85]	0.00 vs KBr(s)[85]
KCl	rock salt ($Fm\bar{3}m$)	O_h	47.80 vs KCl(aq)[85]	0.00 vs KCl(s)[85]
KF	rock salt ($Fm\bar{3}m$)	O_h	22.60 vs KCl(aq)[85]	0.00 vs KF(s)[85]
MgO	rock salt ($Fm\bar{3}m$)	O_h	26 ± 1 vs MgSO$_4$ (aq)[86] 26.26 ± 0.05 vs Mg(NO$_3$)$_2$(aq)[87]	
MgS	rock salt ($Fm\bar{3}m$)	O_h	−3 ± 1 vs MgSO$_4$ (aq)[86] −1.11 ± 0.02 vs Mg(NO$_3$)$_2$ (aq)[87]	
ZnS	zinc blende ($F\bar{4}3m$)	T_d	−378 vs ZnSO$_4$ (aq)[88] −380.5 vs ZnSO$_4$ (aq)[88]	
ZnSe	zinc blende ($F\bar{4}3m$)	T_d	−273 vs ZnSO$_4$ (aq)[88] −276.3 vs ZnSO$_4$ (aq)[88]	

exist.[104−107] The experimental data of the chemical shifts δ is listed in Table 1 together with the local coordination environment around the metal or halide/chalcogenide centers. The used bond length as well as a comparison to the bond length of periodic calculations can be found in the Supporting Information in Table S2.

In the following, this wide variety of chemical shifts will be used to evaluate the performance of DFT, MP2, and double-hybrid methods in computing NMR NSCs.

4. CONSTRUCTION OF CLUSTER MODELS

The NMR NSC calculations on the chosen set of inorganic solids were performed in the framework of embedded cluster calculations. This requires sufficiently large quantum clusters (QCs), which are extracted from the respective crystallographic supercells. As it has been discussed recently,[108] the quantum clusters can be extracted by either employing a "supercell" (SCe) approach, in which the resulting clusters contain building units that correspond to the crystallographic unit cell, or employing a "spherical cluster" (SCl) approach, whereby the cluster expands spherically around a chosen center with complete coordination (i.e., O_h or tetrahedral T_d in the rock salt or zinc blende systems, respectively). Both approaches should ultimately lead to the same results for a given property. In Figure 1, both the embedding approaches for SCe and SCl are presented for the case of NaCl. The
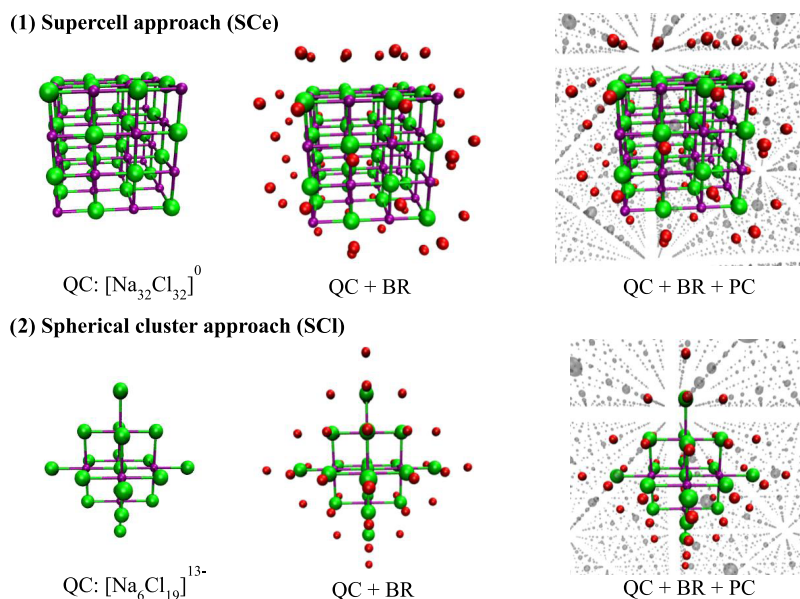
Figure 1. Graphical representation of the embedded cluster approach for NaCl. (1) Supercell approach (SCe). (2) Spherical cluster approach (SCl). Color coding: QC: Na (purple); Cl (green). BR: cECPs (red). PC (gray).

nomenclature and color code for the different positions in the QC are shown in Figure 2.
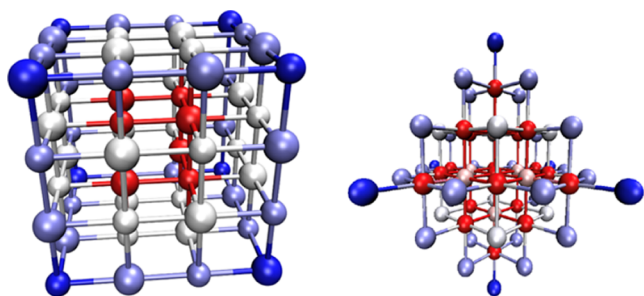
Figure 2. Nomenclature for the example of the $[Na_{32}Cl_{32}]^0$ and $[Na_{19}Cl_{44}]^{25-}$ quantum clusters. Centers with different chemical environments are denoted with color coding: tip (dark blue), edge (light purple), facets (gray), and bulk (red). Small spheres: Na; large spheres: Cl.

As shown in Figure 1, the QCs are embedded in a point charge (PC) field of about 10 000 charges, which accounts for the long-range Coulomb effects. The charges are at the positions of the cations (positive charges) and anions (negative charges) based on the crystallographic data. Capping effective core potentials (cECPs) together with a charge are introduced between the QC and PC regions as a boundary region (BR) to avoid spurious electron leakage and overdelocalization from the QC clusters. In particular, an up to triple layer of cECPs— ECP2SDF (Li, O, F),[109] ECP10SDF (Mg, Na),[110] ECP10MDF (Zn),[111] ECP10MWB (Cl, S, K),[112] and ECP28MWB (Br, Se)[112] (included in the SDD framework)—was used to replace the corresponding atoms. For the cECPs and PCs, the charges are chosen imposing cluster-neutrality conditions (i.e., $q(QC) = -q(BR + PC)$)[113] and by ensuring uniform charge distribution in the QC, BR, and PC regions. For this purpose, the value of the PCs was matched with the computed electrostatic potential charges (CHELPGs)[114,115] of the QC iteratively until the charges of QC matched the value of the PCs. Further details regarding

Table 2. Quantum Cluster Sizes and Optimized Charges of BR and PCs that Were Employed to Compute the DFT and MP2 NMR NSCs

system	smallest system tested SCl/SCe	largest system tested SCl/SCe	converged size metal SCl/SCe	converged size halide/chalcogenide SCl/SCe	charge
LiBr	$[LiBr_6]^{5-}/[LiBr]^0$	$[Li_{19}Br_{44}]^{25-}/[Li_{62}Br_{62}]^0$	$[Li_6Br_{19}]^{13-}/[Li_{16}Br_{16}]^0$	$[Li_6Br_{19}]^{13-}/[Li_{32}Br_{32}]^0$	±0.79
LiCl	$[LiCl_6]^{5-}/[LiCl]^0$	$[Li_{19}Cl_{44}]^{25-}/[Li_{62}Cl_{62}]^0$	$[Li_6Cl_{19}]^{13-}/[Li_{16}Cl_{16}]^0$	$[Li_{32}Cl_{32}]^{13-}/[Li_{32}Cl_{32}]^0$	±0.95
LiF	$[LiF_6]^{5-}/[LiF]^0$	$[Li_{19}F_{44}]^{25-}/[Li_{62}F_{62}]^0$	$[Li_6F_{19}]^{13-}/[Li_{16}F_{16}]^0$	$[Li_6F_{19}]^{13-}/[Li_{32}F_{32}]^0$	±1.23
NaBr	$[NaBr_6]^{5-}/[NaBr]^0$	$[Na_{19}Br_{44}]^{25-}/[Na_{62}Br_{62}]^0$	$[Na_6Br_{19}]^{13-}/[Na_{16}Br_{16}]^0$	$[Na_6Br_{19}]^{13-}/[Na_{32}Br_{32}]^0$	±0.86
NaCl	$[NaCl_6]^{5-}/[NaCl]^0$	$[Na_{19}Cl_{44}]^{25-}/[Na_{62}Cl_{62}]^0$	$[Na_6Cl_{19}]^{13-}/[Na_{16}Cl_{16}]^0$	$[Na_6Cl_{19}]^{13-}/[Na_{32}Cl_{32}]^0$	±0.93
NaF	$[NaF_6]^{5-}/[NaF]^0$	$[Na_{19}F_{44}]^{25-}/[Na_{62}F_{62}]^0$	$[Na_6F_{19}]^{13-}/[Na_{16}F_{16}]^0$	$[Na_6F_{19}]^{13-}/[Na_{32}F_{32}]^0$	±1.10
KBr	$[KBr_6]^{5-}/[KBr]^0$	$[K_{19}Br_{44}]^{25-}/[K_{62}Br_{62}]^0$	$[K_6Br_{19}]^{13-}/[K_{16}Br_{16}]^0$	$[K_6Br_{19}]^{13-}/[K_{32}Br_{32}]^0$	±0.78
KCl	$[KCl_6]^{5-}/[KCl]^0$	$[K_{19}Cl_{44}]^{25-}/[K_{62}Cl_{62}]^0$	$[K_6Cl_{19}]^{13-}/[K_{16}Cl_{16}]^0$	$[K_6Cl_{19}]^{13-}/[K_{32}Cl_{32}]^0$	±0.90
KF	$[KF_6]^{5-}/[KF]^0$	$[K_{19}F_{44}]^{25-}/[K_{62}F_{62}]^0$	$[K_6F_{19}]^{13-}/[K_{16}F_{16}]^0$	$[K_6F_{19}]^{13-}/[K_{32}F_{32}]^0$	±1.05
MgO	$[MgO_6]^{10-}/[MgO]^0$	$[Mg_{19}O_{44}]^{50-}/[Mg_{62}O_{62}]^0$	$[Mg_6O_{19}]^{26-}/[Mg_{16}O_{16}]^0$	$[Mg_6O_{19}]^{26-}/[Mg_{32}O_{32}]^0$	±1.70
MgS	$[MgS_6]^{10-}/[MgS]^0$	$[Mg_{19}S_{44}]^{50-}/[Mg_{62}S_{62}]^0$	$[Mg_6S_{19}]^{26-}/[Mg_{16}S_{16}]^0$	$[Mg_6S_{19}]^{26-}/[Mg_{32}S_{32}]^0$	±1.51
ZnS	$[ZnS_4]^{6-}$	$[Zn_8S_{19}]^{22-}$	$[Zn_4S_{10}]^{12-}$		±0.55
ZnSe	$[ZnSe_4]^{6-}$	$[Zn_8Se_{19}]^{22-}$	$[Zn_4Se_{10}]^{12-}$		±0.50

Table 3. Computed NMR NSCs of Na and Cl in $[NaCl_6]^{5-}$ and $[Na_4Cl_4]^0$ with Different Electrostatic Environments, PBE/pcSseg-2

$[NaCl_6]^{5-}$	no embedding	1-layer cECPs	1-layer cECPs + 1-layer PCs	1-layer cECPs + 2-layer PCs	1-layer cECPs + 10 000 PC
NSC(Na)/ppm	558.74	546.90	550.76	549.82	550.21
NSC(Cl)/ppm	1042.21	1086.66	1091.62	1090.86	1091.18
$[Na_4Cl_4]^0$	no embedding	1-layer cECPs	1-layer cECPs + 1-layer PCs	1-layer cECPs + 2-layer PCs	1-layer cECPs + 10 000 PCs
NSC(Na)/ppm	570.76	583.77	583.61	583.63	583.63
NSC(Cl)/ppm	1059.61	1085.50	1085.12	1085.17	1085.16

the employed embedding scheme have been described elsewhere.[108] It should be noted that within the employed embedding scheme, the positions and magnitudes of the point charges are kept fixed while no additional corrections for the long-range electrostatics are taken into account.[38] This scheme has been proven successful in treating a variety of chemical problems in the field of semiconductors, insulators as well as molecular crystals.[5–9,108,116–119] Note that while this scheme can be applied to a broad range of systems, metallic systems or materials for which the electronic structure is strongly delocalized cannot be treated and problems might be anticipated for certain polar systems.[38,120]

The impact of the employed embedded cluster approach on the computed NMR NSCs will be discussed in detail in the following section. Details with respect to the size of the constructed cluster, as well as the magnitude of the optimized charges in the BR and the PC regions, are provided in Table 2.

5. DEPENDENCE OF THE NUCLEAR SHIELDING CONSTANT ON DIFFERENT MODEL PARAMETERS

Prior to the evaluation of the performance of DFT and MP2 approaches to compute experimental NMR chemical shifts in the chosen set of inorganic solids, we investigated in detail the case of NaCl. In this section, in particular, we will investigate (a) the influence of electrostatic embedding on the electronic structure of the resulting embedded cluster and (b) the actual size of the employed quantum cluster (QC) required to arrive at converged values of computed NMR NSCs. The aim is to be able to obtain results for solid materials with the accuracy that molecular post-HF and double-hybrid DFT approaches offer. Hence, the cluster size and embedding scheme should be converged to errors smaller than the inherent to the method or the basis set.

5.1. Influence of Electrostatic Embedding. At first, we analyze the electronic structure of various constructed cluster models in terms of orbital energies and partial charges. For this purpose, the bare and embedded SCe ($[NaCl_6]^{5-}$) and SCl ($[Na_4Cl_4]^0$) quantum clusters are employed.

At the PBE/pcSseg-2 level of theory, the highest occupied molecular orbital (HOMO) of the charged quantum cluster $[NaCl_6]^{5-}$ has an energy of 64.07 eV and the lowest occupied molecular orbital (LUMO) lies at 67.36 eV. Without embedding an unphysical positive energy of the HOMO arises due to the high charge of the bare cluster, which will have detrimental effects on all calculations. Not only would it yield erratic properties, but in many cases calculations would not even converge. By embedding the quantum clusters in a boundary region with one-layer cECPs and a point charge field with ~10 000 point charges, the HOMO and LUMO energies shift to −6.86 and 1.07 eV, respectively. The overall HOMO–LUMO gap increases from 3.28 to 7.93 eV. This value is closer to the value of the experimental band gap of the solid NaCl (8.97 eV[108]) and hence gives already a better description of the

electronic structure of the solid. On the contrary, the electrostatic embedding influence is not as pronounced for the charge-neutral $[Na_4Cl_4]^0$ quantum cluster. The HOMO shifts from −5.79 to −6.92 eV and the LUMO from −1.52 to 0.62 eV. As is seen in Table 3, the charged quantum cluster $[NaCl_6]^{5-}$ requires more PC layers than the charge-neutral quantum cluster $[Na_4Cl_4]^0$ before the NMR NSCs are converged with respect to the embedding size. In fact, for $[Na_4Cl_4]^0$, the result does not change significantly after one PC layer, while three PC layers are needed for $[NaCl_6]^{5-}$. Hence, for consistency, in all studied systems, the quantum clusters were embedded in 10 000 PCs. This is possible since the inclusion of point charges does not have a significant effect on the computation time.

The need of only one PC layer for the neutral $[Na_4Cl_4]^0$ to get a converged NMR NSC result with respect to the size of the embedding field indicates that long-range electrostatic effects do not influence the shielding of the atoms effectively. Only the local effects of the embedding charges on their direct neighbor have a dominant impact from an electrostatic perspective. The core potentials of the boundary region are damping the dangling bonds on the outside of the QC and balancing the charge distribution inside the QC. This is reflected in the variation of the Na and Cl NMR NSCs of the embedded versus bare $[Na_4Cl_4]^0$ and $[NaCl_6]^{5-}$ clusters. In particular, the NMR NSCs of Cl increase for both the embedded $[Na_4Cl_4]^0$ and $[NaCl_6]^{5-}$ clusters in comparison to the nonembedded ones. On the contrary, the NMR NSCs of Na increase in $[Na_4Cl_4]^0$ and decrease in $[NaCl_6]^{5-}$ when the bare clusters are embedded. In the case of $[Na_4Cl_4]^0$, Na is less shielded in the bare cluster because it is on the outside of the cluster and it has a stronger and more covalent bond to Cl. The increase is also caused by the overall higher charge density in the cluster due to the PC field. In the case of $[NaCl_6]^{5-}$, Na is more shielded by Cl in the bare cluster due to the excess of charge.

In a next step, the electrostatic charges of the different cites (top, edge, surface, and bulk) are computed for both the bare and embedded $[Na_{32}Cl_{32}]^0$ QC clusters. Figure 3 shows the convergence of the NSCs of different sites in the cluster with the partial electrostatic charges (CHELPG). It can be seen that the embedding is distributing the charge homogeneously in the cluster, approaching the typical behavior of the solid. The shielding is increasing with a decreasing coordination number (CN)—from the bulk (CN = 8) to the tip (CN = 3) position—in a similar way as in the nonembedded cluster. The overall charge in the QC is higher in the embedded cluster due to the induction of the PCs. Therefore, the shielding is also higher at the tip, edge, and surface positions but not in the bulk position. In the bulk, the NSCs do not significantly differ between embedded and nonembedded clusters (the computed NSCs differ by less than 1.2 ppm). Nevertheless, the electrostatic embedding is still important since it is crucial
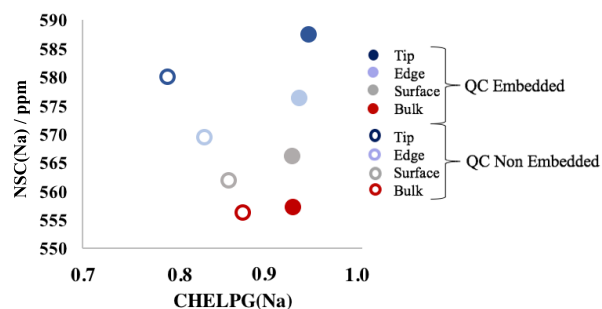
Figure 3. NSCs versus electrostatic charge (CHELPG) distribution on the different quantum cluster ($[Na_{32}Cl_{32}]^0$) centers when the quantum cluster is treated within the embedded approach. QC (embedded) or as a bare neutral cluster (nonembedded).

for the convergence of the cluster, especially for charged systems as for example for those designed with the spherical cluster approach.

Among the different sites, it is the bulk position of the QC that represents the correct chemical environment for the calculation of the NSCs. This makes the size of the QC with regard to shift convergence more crucial than the charge balance itself. The convergence of the cluster size for the different models will be discussed in the next section.

5.2. Convergence of Cluster Size. The convergence and choice of the size of QC will be discussed in the following. For this purpose, different system sizes are studied for the SCe and SCl approaches. A sequence of SCe type of clusters $[Na_nCl_n]^0$, $n = 1-50$, as well as Na-centered $[NaCl_6]^{5-}$, $[Na_2Cl_{10}]^{8+}$, $[Na_4Cl_{16}]^{12-}$, $[Na_6Cl_{19}]^{13-}$, $[Na_{19}Cl_{44}]^{25-}$, and $[Na_{44}Cl_{19}]^{25+}$ and Cl-centered $[Na_6Cl]^{5+}$ $[Na_{10}Cl_2]^{8+}$, $[Na_{16}Cl_4]^{12+}$, $[Na_{19}Cl_6]^{13+}$, $[Na_{44}Cl_{19}]^{25+}$, $[Na_{19}Cl_{44}]^{25-}$, and SCl type of clusters was studied. Representative examples are shown in Figure 4.

As was discussed above for the case of the $[Na_{32}Cl_{32}]^0$ SCe cluster, the computed NMR NSCs of the bulk positions are approximately independent of the embedding (Figure 3). In general, this observation is true for the different sizes of SCe cluster models with the premise that the shift of the bulk is converged (see Figure 5; for just the bulk convergence, see Figure 5c). The already-discussed effects of the embedding (see Section 5.1) lead to a faster convergence of the calculation

and more consistent results compared to the nonembedded clusters. This especially holds true for positions differing from the bulk and is more pronounced for Cl than for Na. The difference can especially be seen for the example of $[Na_{20}Cl_{20}]^0$. The effects of the surface of the QC region influence the shielding of the bulk significantly for the nonembedded system, while this effect cannot be seen for the embedded equivalent.

As seen in Figure 5, the convergence behavior of the computed NMR Na and Cl NSCs is different. In the SCe approach, the Na NSCs of the bulk positions are converged at the $[Na_{16}Cl_{16}]^0$ cluster size, which is the smallest cluster size tested with bulk positions for SCe. The Cl NSCs of the bulk positions are converged at $[Na_{32}Cl_{32}]^0$ cluster size. In the SCl approach, the Na NSCs are considered converged already at the $[NaCl_6]^{5-}$ cluster size as they only differ by about 1 ppm from the next larger cluster size ($[Na_6Cl_{19}]^{13-}$). For Cl, the NSCs are converged at the $[Na_6Cl_{19}]^{13}$ cluster size. This implies that Na only needs one full sphere of Cl. In addition to a full sphere of neighboring Na, the Cl NSC also requires the inclusion of the closest Cl atoms for full convergence. This can especially be seen by building up $[Na_6Cl_{19}]^{13-}$ from $[Na_6Cl]^{5+}$ or the buildup from $[Na_{16}Cl_{16}]^0$ to $[Na_{32}Cl_{32}]^0$. This behavior seems to be linear for the bulk position (see Figure 8b,c). Therefore, the NSC of bulk Cl seems to increase likewise with each additional Cl. Since the difference between $[NaCl_6]^{5-}$ and $[Na_6Cl_{19}]^{13-}$ is not significant, the smaller system could also be used. The differences between $[XY_6]^{5-}$ and $[X_6Y_{19}]^{13-}$ for all metals of the tested rock salt structures are listed in Table S4. For the more ionic systems, the difference is overall not significant. For more covalent systems like MgS, the difference is more pronounced. This behavior offers potentially the opportunity to use smaller systems treated at a higher level of theory, which can be corrected for cluster-size effects. This is in line with recent studies.[121] However, in our view, such corrections are quite empirical and generally not recommended.

Note that the MP2 and DFT (PBE) computed NCSs show similar cluster size convergence behaviors (Figure 5 and 6).

As expected, the Na and Cl NMR NSCs of the Na- and Cl-centered SCl clusters converge toward the bulk Na and Cl centers of the respective SCe clusters (see Figures 5 and 6). In fact, the SCl clusters have a higher bulk-to-surface ratio than
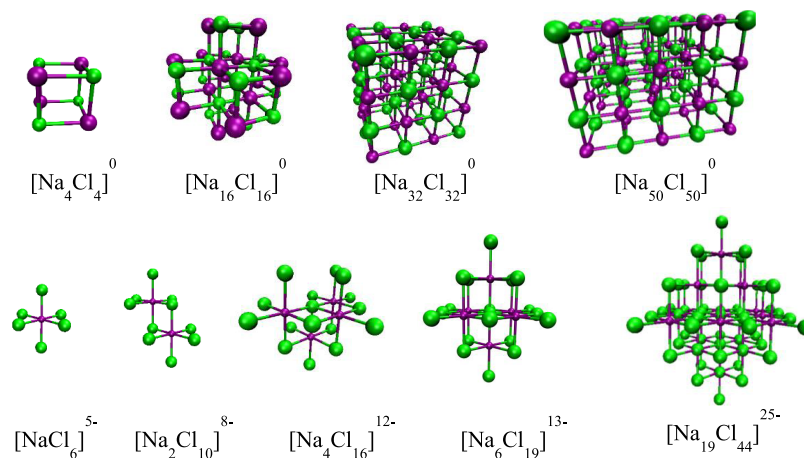
Figure 4. Representative examples of the SCe (top) and SCl (bottom) type of NaCl clusters that were employed to study the cluster-size convergence.
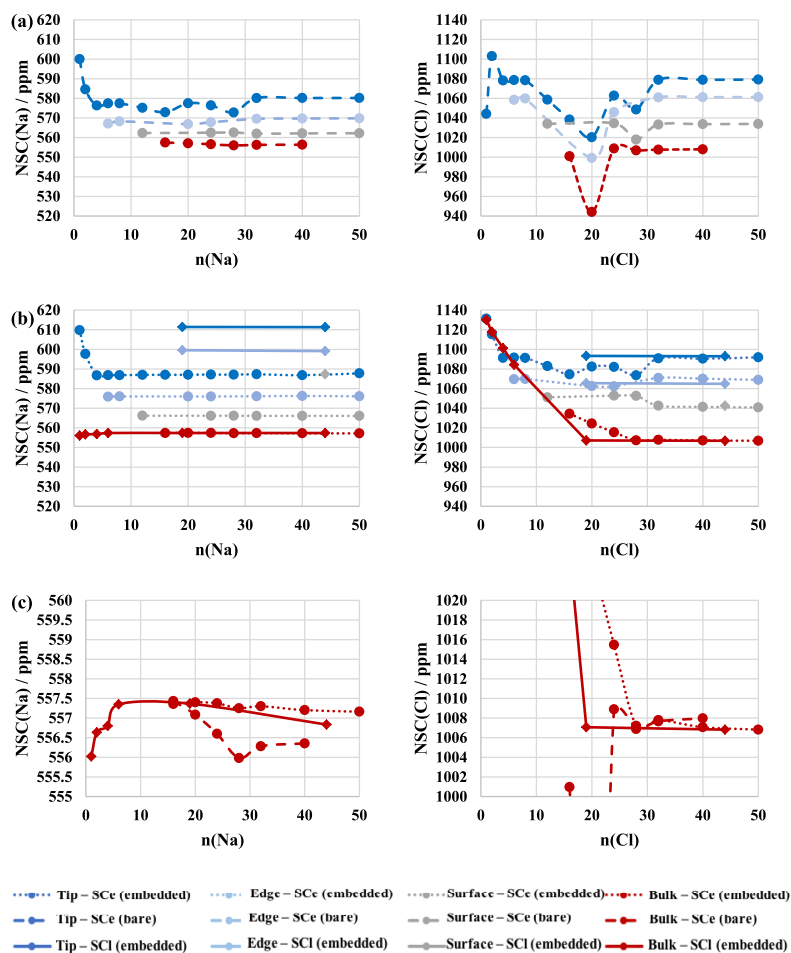
Figure 5. PBE/pcSseg-2-computed NSCs of Na (left) and Cl (right) for NaCl by employing a sequence of (a) bare SCe systems indicated by the dashed line and (b) for the embedded SCe systems indicated by the dotted lines and a sequence of embedded SCl shown with solid lines. (c) Comparison of the shielding effects on both bare (dashed) and embedded (dotted) SCe and embedded SCl (solid line) clusters at the bulk cluster position. The different cluster positions are indicated as tip, blue; edge, light blue; surface, gray; bulk, red.
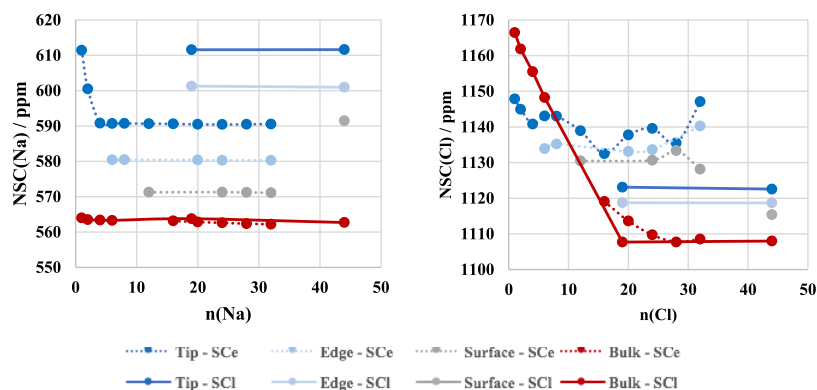
Figure 6. MP2/pcSseg-1-computed NSCs of Na (left) and Cl (right) for NaCl by employing a sequence of embedded SCe- (dotted line) and SCl (solid line)-type clusters. The different cluster positions are indicated as tip, blue; edge, light blue; surface, gray; bulk, red.

the SCe ones. Hence, the SCl systems necessary for convergence are overall smaller. For example, for Cl in NaCl—as for all tested halides in rock salt structures—the converged systems are $[Na_{32}Cl_{32}]^0$ for SCe and $[Na_6Cl_{19}]^{13-}$ for SCl.

The above analysis shows that a criterion of convergence of the cluster size with respect to the computed NCSs cannot be uniquely defined as the range of errors on the computed NCSs

is different in the study set of chosen nuclei and the choice of the type of the embedded clusters (SCl or SCe). However, it becomes evident that as long as sufficiently large clusters are employed, the results are actually insensitive to the chosen embedding scheme.

Based on the above results, one can conclude that the embedding approach in combination with the SCl approach for the construction of the QC clusters leads to an efficient
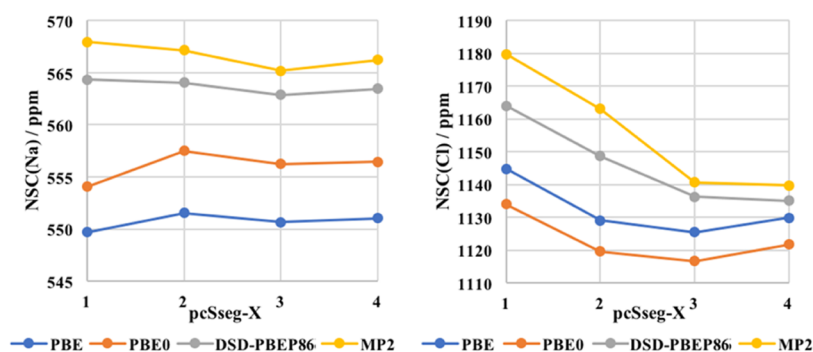
Figure 7. Calculations with different methods—PBE (blue), PBE0 (orange), DSD-PBEP86 (gray), and MP2 (yellow)—for increasing the pcSseg-X basis set size for the NMR NSCs of Na in the embedded systems of $[NaCl_6]^{5-}$ (left) and Cl in $[Na_6Cl]^{5+}$ (right).
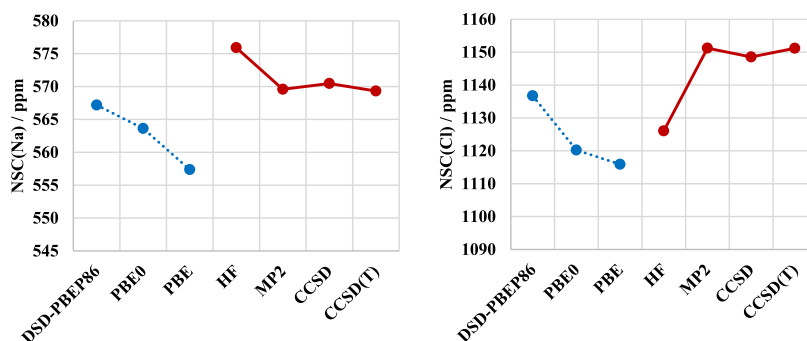
Figure 8. Computed NMR NSCs of Na in $[NaCl_6]^{5-}$ (left) and Cl $[Na_6Cl]^{5+}$ (right) using the pcSseg-2 basis set and for nonembedded clusters. Dotted blue line: PBE, PBE0, DSD-PBEP86; solid red line: HF, MP2, CCSD, CCSD(T).

NMR NSC computational protocol that will be used below to compute the NMR NSCs of the study set of the inorganic solids

6. LEVEL OF THEORY: NUCLEAR SHIELDING CONSTANTS

In the following section, different methods for the computation of NSCs are compared. After assessing the basis set convergence, we compared results for different methods ranging from standard DFT to MP2 and double-hybrid DFT.

6.1. Basis Set Size. To investigate how far the results obtained using a given basis set are from the complete basis set limit for different types of methods, a comparison among PBE, PBE0, DSD-PBEP86, and MP2 is made with increasing pcSseg-X (X = 1−4) basis set size to calculate the NSCs for the central atoms Na and Cl in $[NaCl_6]^{5-}$ or $[Na_6Cl]^{5+}$, respectively (see Figure 7).

For most metals, results obtained using the pcSseg-2 basis set are sufficiently close to the complete basis set limit. This is also the case for most halides, if (meta-)GGA or hybrid functionals are used, but for MP2 and double-hybrid functionals, pcSseg-3 or larger basis sets have to be used. Figure 7 shows that the behavior of DSD-PBEP86 is between that of DFT and MP2. For example, the difference for Cl in $[Na_6Cl]^{5+}$ between pcSseg-2 and pcSseg-3 is for DSD-PBEP86 (12.40 ppm) significantly bigger than for PBE (3.59) and PBE0 (2.87) but smaller than for MP2 (22.30).

Besides the NMR-optimized basis sets, pcSseg-X, cc-pVXZ, and def2-XVPP basis sets were tested. For all basis sets, the NMR NSC approach the same basis set limit as for pcSseg-X if they are decontracted. Only for the contracted pcSseg-X basis sets the results do not differ significantly from their decontracted equivalent. The decontration improves the results but also increases the number of basis sets significantly. The basis set behaviors of contracted and decontracted cc-pVXZ and def2-TZVPP in comparison to pcSseg-X are shown in the Supporting Information in Figure S4. Further information regarding this is provided in the Supporting Information.

Since most systems benefit in general more from a higher pcSseg-X basis set than from decontraction, the contracted basis set pcSseg-3 will be used in the following.

6.2. Residual Error of MP2 and Double-Hybrid DFT with Respect to CCSD(T). While we have demonstrated that novel implementations in combination with embedded cluster approaches allow for GIAO-NMR calculations at the MP2 and double-hybrid DFT level of theory, the question arises as to how far these results are converged with respect to the description of electron correlation. While currently, reference CCSD(T) calculations on large embedded clusters are not yet feasible, we assess this residual error for a smaller benchmark system without embedding.

Figure 8 shows the results for the central atoms Na in nonembedded $[NaCl_6]^{5-}$ and Cl in $[Na_6Cl]^{5+}$. It also shows the result for the GGA functional PBE, the hybrid functional PBE0, and the double-hybrid DSD-PBEP86 to compare convergence in the sense of Perdew's "Jacob's Ladder" of DFT going from GGA to hybrid to double-hybrid functionals. The trend for the embedded systems as well as different basis set sizes is shown in Figure S5 in the Supporting Information. The general trends are not strongly influenced by basis set size or the embedding scheme. The embedding approach is more important for the properties of the atoms on the outside of QC (see previous sections and Table S7a−f in the Supporting Information). CCSD and CCSD(T) have the same basis set

Table 4. Nonrelativistic Computed NCSs and Two-Component Hamiltonian BSS Relativistic Correction for a Series of Nonembedded Model Systems for (a) Halides and (b) Metals[a]

a)	nonrelativistic in ppm	scalar relativistic in ppm	relativistic with SOC in ppm	Δnonrelativistic: scalar relativistic in %	Δnonrelativistic: relativistic with SOC in %
$[Li_6F]^{5+}$	423.4	432.9	433.0	2.24	2.27
$[Na_6F]^{5+}$	441.2	453.7	453.5	2.83	2.79
$[K_6F]^{5+}$	307.9	321.7	321.0	4.48	4.25
$[Li_6Cl]^{5+}$	1095.0	1160.3	1160.5	5.96	5.98
$[Na_6Cl]^{5+}$	1121.7	1189.0	1188.5	6.00	5.96
$[K_6Cl]^{5+}$	985.8	1055.5	1054.4	7.07	6.96
$[Li_6Br]^{5+}$	3025.3	3607.0	3609.0	19.23	19.29
$[Na_6Br]^{5+}$	3081.9	3667.7	3669.1	19.01	19.05
$[K_6Br]^{5+}$	2847.2	3426.2	3427.1	20.34	20.37

b)	nonrelativistic in ppm	scalar relativistic in ppm	relativistic with SOC in ppm	Δnonrelativistic: scalar relativistic in %	Δnonrelativistic: relativistic with SOC in %
$[LiF_6]^{5-}$	121.2	121.6	121.6	0.33	0.41
$[LiCl_6]^{5-}$	97.5	97.9	98.0	0.41	0.51
$[LiBr_6]^{5-}$	95.7	96.2	97.0	0.42	1.36
$[NaF_6]^{5-}$	628.5	646.0	646.0	2.78	2.78
$[NaCl_6]^{5-}$	573.0	590.7	588.0	3.09	2.62
$[NaBr_6]^{5-}$	566.5	584.6	579.4	3.18	2.26
$[KF_6]^{5-}$	1298.3	1387.5	1387.5	6.87	6.87
$[KCl_6]^{5-}$	1281.2	1370.3	1369.1	6.95	6.86
$[KBr_6]^{5-}$	1238.5	1331.8	1317.6	7.53	6.39
$[MgO_6]^{10-}$	560.7	581.6	584.4	3.71	4.21
$[MgS_6]^{10-}$	590.5	612.6	599.2	3.74	1.47
$[ZnS_4]^{6-}$	1560.2	1891.4	1910.8	21.23	22.54
$[ZnSe_4]^{6-}$	1582.9	1923.0	2054.8	21.49	29.81

[a]Level of theory: PBE0/dyall.ae3z.

behavior as MP2 explained in Section 7.3 (see Figure S5a—d and Table S7a—f in the Supporting Information).

The behavior of the wave-function methods shows the importance of correlation effects but also that, in comparison to CCSD(T), MP2 yields remarkably good results. This is in agreement with previous studies, and while it partly is due to error compensation at this level, it implies that calculations with predictive power are feasible at this level of theory.[15,24] The Jacob's Ladder DFT hierarchy has a more monotonous convergence toward the gold standard CCSD(T) results, but only the highest rung of the ladder yields results that approach the quality of higher-order post-HF methods.

6.3. Relativistic Effects. It should be noted that besides the chosen method as the predominant source of error in the computed NCSs, an additional source of error is relativistic effects in the computed chemical shieldings of heavier elements.[122,123] These are presently neglected in our employed protocol. To assess the importance of including relativistic corrections, we investigate their effect in a series of model systems from the alkali metal $[MX_6]^{5-}$/metal halide $[M_6X]^{5+}$ (where M = Li, Na, and K and X = F, Cl, and Br) groups as well as the Mg/Zn transition-metal (TMs) group, namely, the $[MgO_6]^{-10}$, $[MgS_6]^{-10}$, $[ZnS_4]^{-6}$, and $[ZnS_4]^{-6}$ model systems. For this purpose, we applied two-component relativistic Kohn—Sham DFT including spin—orbit coupling, employing the PBE0 functional and the dyall.ae3z basis set. The results are presented in Table 4.

In the case of alkali metal and metal halide model systems, the inclusion of relativistic effects results in an increase of the magnitude of the computed NCSs in the sequence Li to K and F to Br. As expected, the heaviest elements (Zn, Se, and Br) have sizeable effects, which are of heavy-atom effects on the

shielding of the heavy atom (HAHA) and heavy-atom effects on shieldings of light atom (HALA) nature.[124−128]

The HAHA effect is especially pronounced in the relativistic contributions. For example, the NSC values of Br are shifted for the systems LiBr, NaBr, and KBr by about 579−586 ppm and after inclusion of SOC by about 584−580 ppm. As both scalar relativistic and SOC contributions are of similar magnitude across the series, inclusion of relativistic effects is not expected to influence the order of the shifts in the nonrelativistic limit.

The HALA effect, on the other hand, is likely to affect the order of the nonrelativistic NSCs. For the series of Li, for example, inclusion of relativistic effects results in a decrease of the relative shift of NaF with respect to NaBr from 17.5 ppm to up to about 12.8 ppm (see also Tables S10−S12). The scalar relativistic effect of Na itself is quite similar for all three systems (between 17.5 and 18.0 ppm). The effect of SOC decreases the relativistic effect due to the interaction with the halides from the lightest halide to the heaviest one by 0.0 ppm to up to 5.2 ppm. Similar trends are observed in all of the other alkali metal shifts, while similar effects can also be seen for Zn and especially for Zn in combination with Se since both are heavy elements.

While the model systems used to assess the size of relativistic effects have not been embedded and only a two-component method has been applied (see the section about relativistic calculations with DIRAC in the SI for further details—Tables S8−S12 and Figure S6), the numbers given above allow one to estimate when relativistic effects become large enough to qualitatively change the resulting chemical shifts. Hence, one can conclude that the computed relativistic effects certainly have an influence on the NSCs in many cases, but the effect is
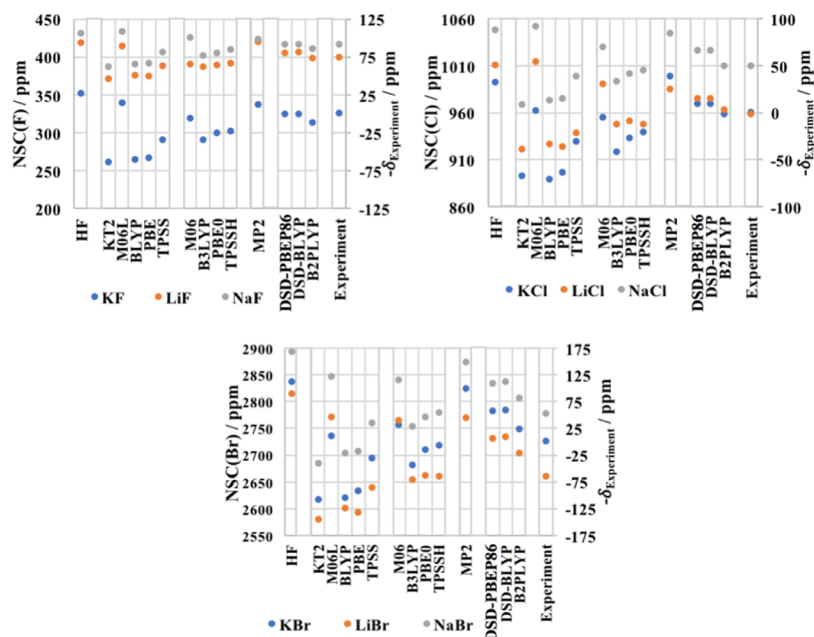
Figure 9. Computed results of NSC for the halides Y in $[X_6Y_{19}]^{13-}$ for (top left) $[X_6F_{19}]^{13-}$, (top right) $[X_6Cl_{19}]^{13-}$, and (bottom) $[X_6Br_{19}]^{13-}$. Computed NSCs (left, primary y-axis) vs experimental chemical shifts (right, secondary y-axis).
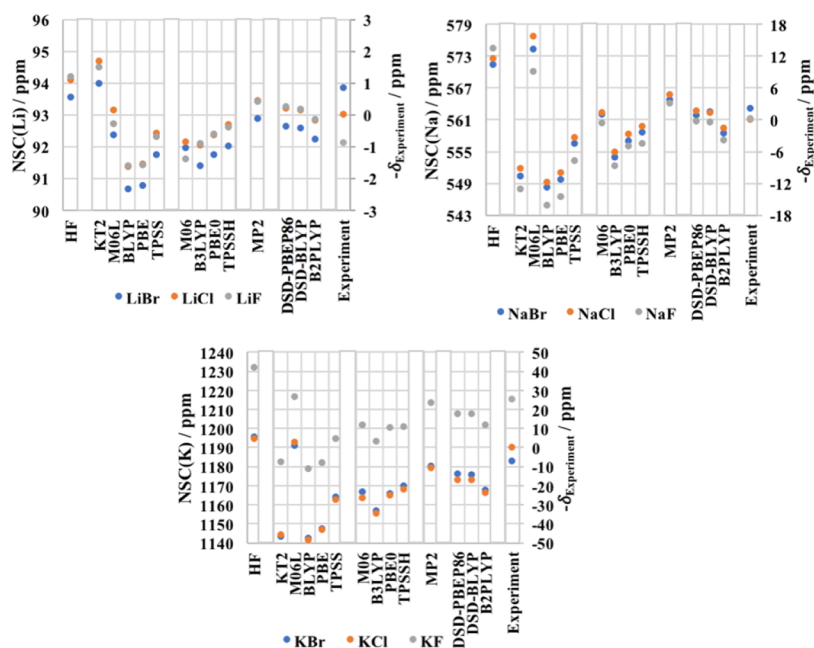
Figure 10. Computed results of NSC for the alkali metals X in $[X_6Y_{19}]^{13-}$ for (top left) $[Li_6Y_{19}]^{13-}$, (top right) $[Na_6Y_{19}]^{13-}$, and (bottom) $[K_6Y_{19}]^{13-}$. Basis set: pcSseg-2. Computed NSCs (left, primary y-axis) vs experimental shifts (right, secondary y-axis).

quite similar within a group of systems. The only significant change for relative shieldings can be expected for light elements interacting with heavy elements, e.g., LiBr or for a system like ZnSe. As, however, the primary focus of this work is to evaluate the performance of the employed embedding protocol to compute NCSs and whether methods with the inclusion of post-HF correlation like MP2 or double-hybrid DFT can be employed in electrostatic embedding schemes without compromising their accuracy, we have chosen to exclude relativistic effects in the following.

7. METHOD DEPENDENCE OF THE COMPUTED NSCS

In a next step, we investigate the method dependence of computed NSCs across the full set of inorganic solids. The results are summarized in Figures 9−11. Since the NSCs are computed as absolute values and the experimental shifts are relative to a standard, we particularly focus on comparing the relative position of the shielding constants and shifts. While the NSCs are given on the primary y-axis (left), the experimental relative values are given on the arbitrarily aligned secondary y-axis (right).

7.1. Method Dependence of Halide Nuclear Shielding Constants. To get good agreement with the experiment, it is
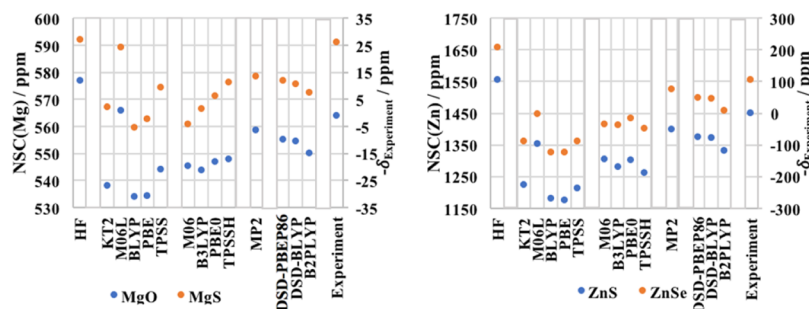
Figure 11. Computed results of NSC for the metals in (left) $[Mg_6Y_{19}]^{26-}$ and (right) $[Zn_4Y_{10}]^{12-}$. Basis set: pcSseg-2. Computed NSCs (left, primary y-axis) vs experimental shifts (right, secondary y-axis).

either required that accurate and robust NSCs are computed or that good error compensations reflected by large deviations of NSCs but small deviations by their difference are given. A comparison of the NSCs allows one to access the situation. In general, better methods should converge to consistent NSC values and accurate chemical shifts as a consequence.

Comparing the results of the NSCs for the different tested halides in Figure 9 shows that in all cases, MP2 and the different double-hybrid functionals give more consistent NSCs compared to hybrid functionals, which outperform (meta-)GGAs in that regard. The range of computed NSCs is the lowest for MP2 and double hybrids. This is especially the case for the potassium halides, which are highly inconsistent for the DFT functionals.

For the example of KCl, the range of computed NSCs with (meta-)GGA, excluding M06L, has a magnitude of about 40.3 ppm; for hybrid functionals, excluding M06, it is 21.3 ppm; and for double-hybrid functionals, it is 11.3 ppm. It should be noted that the observed behavior of M06 is associated with the errors regarding the description of the core region and is consistent with recent discussions.[15,129−131]

For the double hybrids, NaCl and LiCl have a similar range as KCl, making a better error compensation possible. The ranges differ in the cases of hybrid functionals and (meta-)GGAs, leading to more inconsistent results. This can also be seen for F and Br.

Additionally, Hartree−Fock predicts the wrong position of KCl with regard to LiCl and NaCl. This is also reflected in all DFT functionals. And while double-hybrids also give the wrong ordering, MP2 improves the results significantly and yields the correct order.

7.2. Method Dependence of Alkali Metal Nuclear Shielding Constants. In contrast to the highly shielded halides, alkali metals are almost entirely deshielded. Hence, they are very sensitive to small changes in the environment and their experimental chemical shifts often do not differ significantly from each other. For Li and Na for example, the range of chemical shifts $\Delta\delta$ in the experiment is in both cases 2 ppm (see Figure 10). The computed average shielding constant of Li is about 92 ppm and of Na about 560 ppm. An error of 1% of the NSCs in Li would lead to an error of about 46% in the chemical shifts, and an error 1% of the NSCs in Na would lead to an error of about 280% in the chemical shifts. Figure 10 shows that no method predicts the relative positions and the order of the NSCs accurately with respect to experimental chemical shifts. In the case of Li, all of the computed relative NSCs lie within 1 ppm and they deviate from the respective experimental chemical shifts by less than 2 ppm. A similar picture is observed in the case of Na.

Interestingly, the computed NSCs, by employing GGA and meta-GGA functionals, lie within 4−5 ppm; using hybrid functionals, the computed NSCs lie within 3 ppm, while their range drops below 2 ppm in the case of MP2 and double-hybrid functionals. Clearly, in both cases, none of the above-employed methods has the sensitivity to correctly predict such small chemical shift differences.

In the case of K, the relative experimental chemical shifts between KBr and KCl and KCl and KF amount to 7 and 33 ppm. Once again, none of the employed methods is able to correctly predict the order of the KCl and KBr chemical shifts, and this can be attributed in part to the exclusion of relativistic effects from our computational protocol. To investigate this, we discuss in detail the case of the PBE0-computed NCS values for KF, KCl, and KBr. In the nonrelativistic limit, the PBE0-computed NCS values (Figure 10) amount to 1202, 1166, and 1168 ppm for KF, KCl, and KBr, respectively. Inclusion of the relativistic corrections for the model systems $[KF_6]^{5-}$ (89.2 ppm), $[KCl_6]^{5-}$ (87.9 ppm), and $[KBr_6]^{5-}$ (79.1 ppm) in Table 4 results in 1291, 1254, and 1247 ppm for KF, KCl, and KBr, respectively. Hence, at this level of theory, inclusion of relativistic corrections is altering the order of the nonrelativistic NCSs such that agreement with experiment is improved. This implies that a treatment at an even higher level of theory might be required before the magnitude and the order of the computed relative chemical shifts of these highly deshielded nuclei can be correctly computed. However, this goes beyond the scope of the present study; hence, for the time being, double-hybrid and, in particular, the DSD-BLYP-computed chemical shifts (3 and 35 ppm) provide the best agreement with experiment.

7.3. Method Dependence of Magnesium and Zinc Nuclear Shielding Constants. The difficulty of predicting the correct NSCs of MgO and MgS might originate in the different bond characters. Nevertheless, all tested methods predict the correct order of the NSCs (see Figure 11).

In the case of Mg, the experimental chemical shifts between MgO and MgS amount to 28 ppm. All methods predict the order of the MgO and MgS NSCs correctly. HF under-estimates the relative positions of the NSCs of MgO and MgS by about 13 ppm. The results of (meta-)GGA functionals are not systematic for either MgS or MgO. However, the computed shifts lie within 2−3 ppm from the respective experimental chemical shift. The absolute NSCs in the case of MgO are comparable to each other when hybrid functionals are used. This is not the case for MgS, for which the computed NSCs are functional-dependent. Among the hybrid functionals, TPSSH provides a chemical shift that is the closest to the
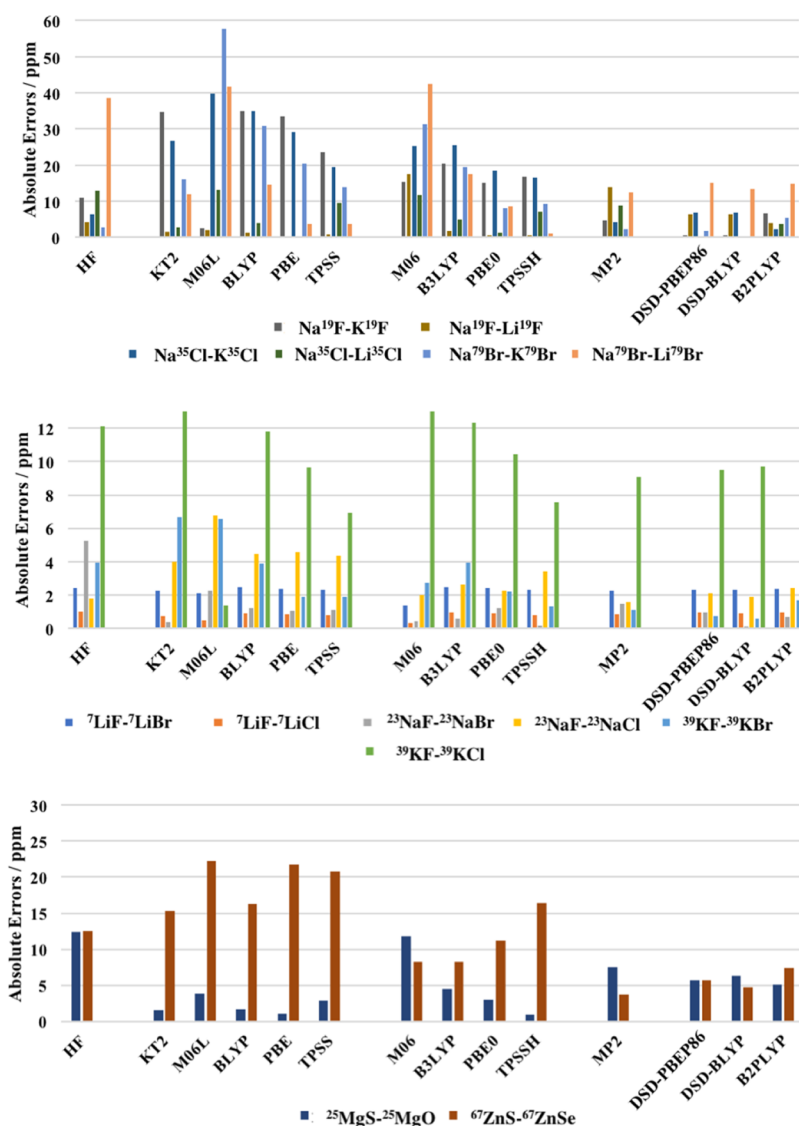
Figure 12. Absolute errors (in ppm) of calculated vs experimental chemical shifts; basis set: pcSseg-3.

experimental value. Both MP2 and double hybrids under-estimate the relative chemical shift by about 5–6 ppm.

For Zn, the experimental chemical shift between ZnS and ZnSe amounts to 104 ppm. All methods predict the order of the ZnS and ZnSe NSCs correctly. HF, the GGA functional M06L, and the hybrid functional M06 provide chemical shifts that are in perfect agreement with the experimental value. However, other GGA and meta-GGA functionals overestimate the relative chemical shift by more than 40 ppm. In the case of hybrid functionals, this value drops below 30 ppm, while in the case of MP2 and double-hybrid functionals, this overestimation decreases further to about 20–22 ppm.

Concluding all studied cases in Sections 7.1–7.3, one can say that in the case of GGA functionals the computed NSCs are strongly method-dependent. This is less pronounced in the case of hybrid functionals, and it is even less pronounced in the case of double-hybrid functionals. In fact, the HF, GGA, meta-GGA, and hybrid functionals show quite large performance variation. While the GGA PBE, the meta-GGA TPSS, and the hybrid functionals PBE0 and TPSSH are found to perform satisfactorily in many cases, MP2 and double-hybrid func-tionals are found to be the most robust in computing NSCs,

while except for the Zn case, they are able to predict experimental ranges of cross-system chemical shifts ($\Delta\delta$) with errors that are below 10 ppm. We anticipate that inclusion of relativistic effects in the computed NCSs, especially for systems bearing heavier elements like Br or Se, will further improve the results. It was shown in Section 7.3 that in the case of metal bromides MBr (M = Li, Na, K) relativistic effects become significant as well as in the case of ZnS and ZnSe. These contributions are expected to become even more pronounced going beyond the fourth row of the periodic table. Never-theless, in our view, improving the employed theoretical methods is primarily important before relativistic corrections can be effectively used to improve the computed chemical shifts.

8. COMPARISON TO EXPERIMENT: CHEMICAL SHIFTS

Typically, NMR experiments report chemical shifts, in which the observed signal is reported relative to a standard compound. Hence, if computed results are to be compared to experiment, relative values need to be evaluated. This causes error compensation in some cases but can also increase the

Table 5. (a) Mean Absolute Error and (b) Mean Deviation for the Different Methods and Nuclei (Orange: Worst Two and Green: Best Two Values for Each Nucleus)[a]

(a)	HF	KT2	M06L	BLYP	PBE	TPSS	M06	B3LYP	PBE0	TPSSH	MP2	DSD-PBEP86	DDSD-BLYP	B2PLYP	Δδ	~NSC
^{7}Li	1.7	1.5	1.3	1.7	1.6	1.5	0.9	1.7	1.7	1.6	1.6	1.6	1.6	1.6	2	90
^{23}Na	3.5	2.2	4.5	2.8	2.8	2.7	1.2	1.6	1.7	1.8	1.5	1.5	0.9	1.6	2	500
^{39}K	8.0	9.9	4.0	7.9	5.8	4.4	7.9	8.1	6.3	4.4	5.1	5.1	5.1	5.9	32	1100
^{19}F	7.7	18.1	2.2	18.2	16.9	12.3	16.5	11.2	7.9	8.8	9.3	3.5	3.5	5.3	91	400
^{35}Cl	9.7	14.8	26.5	19.4	14.7	14.5	18.5	15.3	9.9	11.7	6.5	3.4	3.6	3.0	55	1000
^{79}Br	20.7	14.0	49.7	22.7	12.2	8.9	36.8	18.5	8.3	5.3	7.4	8.4	6.8	10.2	120	2800
^{25}Mg	12.5	1.6	3.8	1.7	1.0	2.8	11.8	4.5	3.0	0.9	7.5	5.7	6.3	5.1	28	500
^{67}Zn	12.6	15.3	22.3	16.2	21.8	20.7	8.2	8.3	11.2	16.4	3.8	5.7	4.7	7.3	104	1300

(b)	HF	KT2	M06L	BLYP	PBE	TPSS	M06	B3LYP	PBE0	TPSSH	MP2	DSD-PBEP86	DDSD-BLYP	B2PLYP	Δδ	~NSC
^{7}Li	0.7	0.8	0.8	0.8	0.8	0.8	0.5	0.7	0.7	0.8	0.7	0.7	0.7	0.7	2	90
^{23}Na	2.6	2.0	3.4	2.2	2.3	2.2	1.0	1.3	1.1	1.7	0.8	1.1	0.9	1.2	2	500
^{39}K	7.1	8.0	3.4	5.6	3.5	2.2	6.9	6.8	5.2	2.7	4.3	4.0	4.2	4.7	32	1100
^{19}F	4.1	8.2	2.6	10.4	11.2	7.9	8.6	4.2	4.1	4.4	4.0	4.4	4.6	4.2	91	400
^{35}Cl	10.7	15.6	26.5	19.5	17.9	17.2	18.5	15.7	11.0	14.4	5.4	8.2	8.4	10.3	55	1000
^{79}Br	14.5	13.2	47.8	21.8	11.7	7.5	30.9	16.3	6.8	4.8	3.7	5.6	3.6	7.6	120	2800

[a]Basis set: pcSseg-3. Range of chemical shifts for each nucleus: Δδ; and approximate magnitude computed nuclear shielding constants: ~NSC. All values are in ppm.

error depending on which compound and reference compound are chosen. As a result, the choice of reference also introduces some bias into the comparison. In a last step of our analysis, computed chemical shifts, defined as the NSC differences between reference and target compounds, are compared to experimental chemical shifts. As in a given sequence each system can serve as reference for the other systems, the various combinations of target-reference chemical shifts are listed in Figure 12 and Table 5. The different experimental chemical shifts are provided in Table 1. The mean absolute errors (MAEs) of the computed chemical shifts with respect to the experimental ones are provided in Figure 12 and Table 5a, while the mean deviations are provided in Table 5b for the different nuclei. As an example, from the metal halides, we discuss the case of F chemical shift errors of NaF with respect to KF and LiF standards. One can see that for KF-NaF the absolute errors of the computed chemical shifts vary between 35 and 1 ppm across the different DFT functionals, HF and MP2. For LiF-NaF, the respective errors vary between 15 and 2 ppm, showing different error distributions with respect to KF-NaF. A similar picture is observed for all of the studied cases presented in Figure 12. Another characteristic example

from the metal halides are the K chemical shifts of KF with respect to the KCl and KBr standards. One can see that while for KCl-KF the errors on the computed chemical shifts are always higher than 6.5 ppm, in the case of KBr-KF the errors vary between 6.5 and 0.8 ppm across the different DFT functionals, HF and MP2. Despite this bias effect, the errors in the computed chemical shifts are largely dominated by the employed method.

Based on the results presented in Figure 12 and Table 5, the mean absolute error is the lowest for MP2 and double hybrids. The double hybrids have overall smaller errors than MP2 and seem to have very similar performance independent of the functional. This is different for hybrids and (meta-)GGAs. Especially M06L and M06 seem to give very inconsistent results. TPSSH and PBE0, as mentioned before, have low errors, too.

As discussed in the previous section, although the chemical shift of the alkali metals is predicted wrong, the absolute error is not high in comparison to the computed NSCs although it is high relative to the shifts. The mean absolute error for these elements is overall, for all methods, the lowest. There is no significant difference between the different classes, but MP2

and double hybrids as well as TPSSH, PBE0, TPSS, and PBE give slightly better results.

For the halides, the range of shifts is bigger and the NSCs are higher. The MAEs are more dependent on the methods. In general, (meta-)GGAs are significantly worse than hybrid functionals with PBE0 and TPSSH performing the best for this class. Double hybrids perform significantly better than hybrid functionals. In most cases, the errors decrease slightly from MP2 to double hybrids.

For magnesium, the error is the most consistent for the different double hybrids and similar for MP2, but hybrid functionals and (meta-)GGAs seem to perform better with regard to MAE. The MAE trend of zinc is similar to the one of halides, with MP2 being slightly better than double hybrids in the tested case.

The result that double-hybrid functionals outperform other DFT functionals using GIAOs to compute NMR parameters is in agreement with prior results for molecules.[15] This shows that the methods for molecular systems can be transferred to the solid state using the electrostatic embedding approach with comparable accuracy. If methods including post-HF correlation are applied, the residual errors amount to only a few percent, and other effects become more important, like relativistic corrections and zero-point vibration corrections. These effects have been omitted as they go beyond the scope of the present study. It was shown, however, that for example relativistic effects might become important in the case of chemical systems containing Br and Se atoms, and it not only alters the results of the heavy nuclei but can influence the shieldings of light nuclei as well.

9. CONCLUSIONS

In this work, we have explored the possibility of combining efficient DFT, MP2, and double-hybrid DFT algorithms for molecular systems with an electrostatic embedding procedure. The results demonstrate that this combination allows one to carry the improved accuracy in predictions of NSCs of double-hybrid DFT functionals and MP2 to the computation of crystalline systems.

For this purpose, a series of benchmark systems have been chosen that emphasize long-range Coulombic effects and subtle differences in the electronic structure. Especially the alkali metal halides prove to be particularly difficult, as halide NMR shieldings are known to be difficult properties for electronic structure theory and the alkaline metals are strongly deshielded, yielding very small differences between the shieldings of Li, Na, and K. In the design of the cluster model, we use large point charge fields for the long-range electrostatics, a large quantum cluster, and a boundary region between the point charges and the quantum region consisting of a layer of core potentials. We prioritize a balanced electrostatic description in the three regions of the model and choose the point charges and core potentials in a way to minimize charge differences between the QM and embedding regions. This way, problems with converging calculations of highly charged QM clusters can be avoided and a more consistent model of the solid is obtained. However, the overall influence of the embedding on the NSCs is surprisingly small, given a sufficiently large quantum cluster is used. For the QM cluster itself, a spherical model around the atom of interest yields the fastest convergence for the systems studied here, which is achieved after a shell of neighboring atoms is included. More covalent systems might require somewhat

larger clusters, as we observe for MgS. Overall, it is important to only regard the NMR shieldings of the innermost atoms, as those naturally show the properties closest to bulk behavior. However, the shieldings of the other atoms in the system give useful information about the residual error due to size convergence of the cluster.

In agreement with previous results, we find that a good balance of efficiency and accuracy is achieved applying Jensen's pcSseg-3 basis set, while the smaller pcSseg-2 basis set might be used in conjunction with GGA and hybrid DFT. As has been shown for a series of properties, MP2 and double-hybrid DFT show a somewhat slower basis set convergence than standard DFT, thus requiring somewhat larger basis sets.

A study on small cluster structures without embedding shows that for the benchmark systems chosen in this study, MP2 results are fairly close to values obtained at the CCSD(T) level of theory.

Finally, we compared chemical shifts computed at several levels of theory, including common (meta-)GGA (KT2, M06L, BLYP, PBE, and TPSS), hybrid (M06, B3LYP, PBE0, and TPSSH), and double-hybrid functionals (DSD-PBEP86, DSD-BLYP, and B2PLYP) and MP2, to experiment. The results confirm the trend that is also found by comparison of NSC values obtained at various levels of theory. Generally, (meta-)GGA functionals yield results with acceptable accuracy but somewhat larger deviations, with TPSS exhibiting the best performance. Hybrid functionals, in comparison, yield results with slightly improved robustness (lower standard deviations) in many cases, but still some outliers can be found. MP2 and double-hybrid functionals, on the other hand, yield a significant improvement of the results over standard DFT. MP2 and double-hybrid functionals give more consistent results for all nuclei, while most DFT functionals perform significantly different for different nuclei (e.g., M06L). In particular, maximum deviations are reduced and low or the lowest mean deviations are observed for almost all nuclei in the study.

It should be emphasized that as sufficiently large clusters are chosen, the scheme is found to have a remarkably small impact on the results compared to other inherent sources of error like the choice of method or basis set. This is important, as it implies that, provided that the quantum region is sufficiently large, one does not need more elaborate schemes to account for most long-range interactions in the solid.

Hence, we conclude that applying sufficiently large clusters and a balanced electrostatic embedding in conjunction with GIAO-NMR shielding calculations at the MP2 or double-hybrid DFT/pcSseg-3 level of theory allows one to obtain superior accuracy in the prediction of solid-state NMR chemical shifts. This paves the way for more efficient or refined methods like DLPNO-MP2 and CCSD(T) to be used together with the employed NMR protocol to address challenging problems in solid-state NMR, for which the predictive power of post-HF methods is required. However, it is important not to forget that heavy elements require inclusion of relativistic effects and that maybe even zero-point vibrational corrections need to be included to further improve accuracy and narrow deviations from experiment. Especially if elements beyond the late fourth period are included, consideration of scalar relativistic effects and spin−orbit coupling becomes increasingly important.

ASSOCIATED CONTENT

Ⓢ Supporting Information

The Supporting Information is available free of charge at https://pubs.acs.org/doi/10.1021/acs.jctc.0c00067.

Models of the studied solids; list for the benchmark set with structural parameters; comparison of NSCs with lattice constant of periodic calculations with experimental lattice constant; change of NSC by changing the lattice constant; computed NSCs for MgS for sequences of SCe and SCl; study of basis sets (differences of NSCs computed with pcSseg-2 by changing the system size and a comparison of different contracted and decontracted basis set types); computed NSCs with respect to the methods for nonembedded and embedded clusters; comparison among HF, MP2, and CCSD(T); and relativistic calculations with DIRAC (input examples for DIRAC calculations, influence of basis set size on relativistic effect, influence of the model size on relativistic effect, comparison of nonrelativistic NSCs computed with different programs (Orca and DIRAC19) and methods, total relativistic effect computed with different methods, scalar relativistic effect computed with different methods, spin−orbit coupling effect computed with different methods) (PDF)

AUTHOR INFORMATION

Corresponding Authors

Alexander A. Auer − *Max-Planck-Institut für Kohlenforschung, Kaiser-Wilhelm-Platz 1, 45470 Mülheim an der Ruhr, Germany;* ⓞ orcid.org/0000-0001-6012-3027; Email: alexander.auer@kofo.mpg.de

Frank Neese − *Max-Planck-Institut für Kohlenforschung, Kaiser-Wilhelm-Platz 1, 45470 Mülheim an der Ruhr, Germany;* ⓞ orcid.org/0000-0003-4691-0547; Email: frank.neese@kofo.mpg.de

Authors

Anneke Dittmer − *Max-Planck-Institut für Kohlenforschung, Kaiser-Wilhelm-Platz 1, 45470 Mülheim an der Ruhr, Germany*

Georgi L. Stoychev − *Max-Planck-Institut für Kohlenforschung, Kaiser-Wilhelm-Platz 1, 45470 Mülheim an der Ruhr, Germany*

Dimitrios Maganas − *Max-Planck-Institut für Kohlenforschung, Kaiser-Wilhelm-Platz 1, 45470 Mülheim an der Ruhr, Germany*

Complete contact information is available at:
https://pubs.acs.org/10.1021/acs.jctc.0c00067

Notes

The authors declare no competing financial interest.

ACKNOWLEDGMENTS

REFERENCES

(1) Bloch, F.; Hansen, W. W.; Packard, M. Nuclear Induction. *Phys. Rev.* **1946**, 69, No. 127.

(2) Purcell, E. M.; Torrey, H. C.; Pound, R. V. Resonance Absorption by Nuclear Magnetic Moments in a Solid. *Phys. Rev.* **1946**, 69, 37−38.

(3) Takeda, K.; Webb, G. A. *Chapter Two - Solid-State Covariance NMR Spectroscopy*; Academic Press, 2015; Vol. 84, pp 77−113.

(4) True, N. S.; Lindon, J. C. Gas Phase Applications of NMR Spectroscopy. *Encyclopedia of Spectroscopy and Spectrometry*, 1999; pp 660−667.

(5) Lindon, J. C. *In Vivo NMR Methods*; Academic Press, 1999.

(6) Bühl, M.; Malkin, V. G.; Kaupp, M. *Calculation of NMR and EPR Paramaters, Theory and Applications.*; Wiley-VCH Verlag GmbH & Co. KGaA: Weinheim, 2004.

(7) Bühl, M.; van Mourik, T. NMR Spectroscopy: Quantum-Chemical Calculations. *Wiley Interdiscip. Rev.: Comput. Mol. Sci.* **2011**, 1, 634−647.

(8) Grimme, S.; Bannwarth, C.; Dohm, S.; Hansen, A.; Pisarek, J.; Pracht, P.; Seibert, J.; Neese, F. Fully Automated Quantum-Chemistry-Based Computation of Spin−Spin-Coupled Nuclear Magnetic Resonance Spectra. *Angew. Chem., Int. Ed.* **2017**, 56, 14763−14769.

(9) Helgaker, T.; Jaszuński, M.; Ruud, K. Ab Initio Methods for the Calculation of NMR Shielding and Indirect Spin−Spin Coupling Constants. *Chem. Rev.* **1999**, 99, 293−352.

(10) Laskowski, R.; Blaha, P.; Tran, F. Assessment of DFT Functionals with NMR Chemical Shifts. *Phys. Rev. B: Condens. Matter* **2013**, 87, No. 195130.

(11) Ditchfield, R. Self-consistent perturbation theory of diamagnetism. *Mol. Phys.* **1974**, 27, 789.

(12) Wolinski, K.; Hinton, J. F.; Pulay, P. Efficient Implementation of the Gauge-Independent Atomic Orbital Method for NMR Chemical Shift Calculations. *J. Am. Chem. Soc.* **1990**, 112, 8251.

(13) Häser, M.; Ahlrichs, R.; Baron, H.; Weis, P.; Horn, H. Direct computation of second-order SCF properties of large molecules on workstation computers with an application to large carbon clusters. *Theor. Chim. Acta* **1992**, 83, 455.

(14) Wolff, S. K.; Ziegler, T. Calculation of DFT-GIAO NMR shifts with the inclusion of spin-orbit coupling. *J. Chem. Phys.* **1998**, 109, No. 895.

(15) Stoychev, G. L.; Auer, A. A.; Neese, F. Efficient and Accurate Prediction of Nuclear Magnetic Resonance Shielding Tensors with Double-Hybrid Density Functional Theory. *J. Chem. Theory Comput.* **2018**, 14, 4756−4771.

(16) Gauss, J. Effects of electron correlation in the calculation of nuclear magnetic resonance chemical shifts. *J. Chem. Phys.* **1993**, 99, No. 3629.

(17) Kollwitz, M.; Gauss, J. A direct implementation of the GIAO-MBPT(2) method for calculating NMR chemical shifts. Application to the naphthalenium and anthracenium ions. *Chem. Phys. Lett.* **1996**, 260, 639.

(18) Kollwitz, M.; Häser, M.; Gauss, J. Non-Abelian point group symmetry in direct second-order many-body perturbation theory calculations of NMR chemical shifts. *J. Chem. Phys.* **1998**, 108, No. 8295.

(19) Gauss, J. GIAO-MBPT(3) and GIAO-SDQ-MBPT(4) Calculations of Nuclear Magnetic Shielding Constants. *Chem. Phys. Lett.* **1994**, 229, 198.

(20) Gauss, J.; Stanton, J. F. Coupled-Cluster Calculations of Nuclear Magnetic Resonance Chemical Shifts. *J. Chem. Phys.* **1995**, 103, No. 3561.

(21) Gauss, J.; Stanton, J. F. Gauge Invariant Calculation of Nuclear Magnetic Shielding Constants at the Coupled-Cluster Singles and Doubles Level. *J. Chem. Phys.* **1995**, 102, No. 251.

(22) Gauss, J.; Stanton, J. F. Perturbative Treatment of Triple Excitations in Coupled Cluster Calculations of Nuclear Magnetic Shielding Constants. *J. Chem. Phys.* **1996**, 104, No. 2574.

(23) Gauss, J.; Stanton, J. F. Analytic CCSD(T) second derivatives. *Chem. Phys. Lett.* **1997**, *276*, 70−77.

(24) Flaig, D.; Maurer, M.; Hanni, M.; Braunger, K.; Kick, L.; Thubauville, M.; Ochsenfeld, C. Benchmarking Hydrogen and Carbon NMR Chemical Shifts at HF, DFT, and MP2 Levels. *J. Chem. Theory Comput.* **2014**, *10*, 572−578.

(25) Helgaker, T.; Coriani, S.; Jørgensen, P.; Kristensen, K.; Olsen, J.; Ruud, K. Recent Advances in Wave Function-Based Methods of Molecular-Property Calculations. *Chem. Rev.* **2012**, *112*, 543−631.

(26) Gauss, J.; Werner, H. J. NMR Chemical Shift Calculations within Local Correlation Methods: The GIAO-LMP2 Approach. *Phys. Chem. Chem. Phys.* **2000**, *2*, 2083.

(27) Loibl, S.; Schütz, M. NMR Shielding Tensors for Density Fitted Local Second-Order Møller-Plesset Perturbation Theory Using Gauge Including Atomic Orbitals. *J. Chem. Phys.* **2012**, *137*, No. 084107.

(28) Ochsenfeld, C.; Kussmann, J.; Koziol, F. Ab Initio NMR Spectra for Molecular Systems with a Thousand and More Atoms: A Linear-Scaling Method. *Angew. Chem., Int. Ed.* **2004**, *43*, 4485.

(29) Kussmann, J.; Ochsenfeld, C. Linear-Scaling Method for Calculating Nuclear Magnetic Resonance Chemical Shifts Using Gauge-Including Atomic Orbitals within Hartree-Fock and Density-Functional Theory. *J. Chem. Phys.* **2007**, *127*, No. 054103.

(30) Beer, M.; Kussmann, J.; Ochsenfeld, C. Nuclei-Selected Nmr Shielding Calculations: A Sublinear-Scaling Quantum-Chemical Method. *J. Chem. Phys.* **2011**, *134*, No. 074102.

(31) Keal, T. W.; Tozer, D. J. The Exchange-Correlation Potential in Kohn−Sham Nuclear Magnetic Resonance Shielding Calculations. *J. Chem. Phys.* **2003**, *119*, 3015−3024.

(32) Reimann, S.; Ekström, U.; Stopkowicz, S.; Teale, A. M.; Borgoo, A.; Halgaker, T. The importance of current contributions to shielding constants in density-functional theory. *Phys. Chem. Chem. Phys.* **2015**, *17*, 18834.

(33) Stoychev, G. L.; Auer, A. A.; Izsák, R.; Neese, F. Self-Consistent Field Calculation of Nuclear Magnetic Resonance Nuclear shielding Constants Using Gauge-Including Atomic Orbitals and Approximate Two-Electron Integrals. *J. Chem. Theory Comput.* **2018**, *14*, 619.

(34) Charpentier, T. The PAW/GIPAW Approach for Computing NMR Parameters: A New Dimension Added to NMR Study of Solids. *Solid State Nucl. Magn. Reson.* **2011**, *40*, 1−20.

(35) de Wijs, G. A.; Laskowski, R.; Blaha, P.; Havenith, R. W. A.; Kresse, G.; Marsman, M. NMR Shielding constants from Density Functional Perturbation Theory: GIPAW Versus All-Electron Calculations. *J. Chem. Phys.* **2017**, *146*, No. 064115.

(36) Pickard, C. J.; Mauri, F. All-Electron Magnetic Response with Pseudopotentials: NMR Chemical Shifts. *Phys. Rev. B: Condens. Matter* **2001**, *63*, No. 245101.

(37) Blöchl, P. E. Projector Augmented-Wave Method. *Phys. Rev. B* **1994**, *50*, 17953−17979.

(38) Weber, J.; Schmedt auf der Günne, J. Calculation of NMR Parameters in Ionic Solids by an Improved Self-Consistent Embedded Cluster Method. *Phys. Chem. Chem. Phys.* **2010**, *12*, 583−603.

(39) Hartman, J. D.; Kudla, R. A.; Day, G. M.; Mueller, L. J.; Beran, G. J. O. Benchmark Fragment-Based 1H, 13C, 15N and 17O Chemical Shift Predictions in Molecular Crystals. *Phys. Chem. Chem. Phys.* **2016**, *18*, 21686−21709.

(40) Sebastiani, D.; Rothlisberger, U. Nuclear Magnetic Resonance Chemical Shifts from Hybrid DFT QM/MM Calculations. *J. Phys. Chem. B* **2004**, *108*, 2807−2815.

(41) Krykunov, M.; Ziegler, T.; van Lenthe, E. Implementation of a Hybrid DFT Method for Calculating NMR Shieldings Using Slater-Type Orbitals with Spin−Orbital Coupling Included. Applications to 187Os, 195Pt, and 13C in Heavy-Metal Complexes. *J. Phys. Chem. A* **2009**, *113*, 11495−11500.

(42) Neese, F.; Atanasov, M.; Bistoni, G.; Maganas, D.; Ye, S. Chemistry and Quantum Mechanics in 2019: Give Us Insight and Numbers. *J. Am. Chem. Soc.* **2019**, *141*, 2814−2824.

(43) Thonhauser, T.; Ceresoli, D.; Mostofi, A. A.; Marzari, N.; Resta, R.; Vanderbilt, D. A converse approach to the calculation of NMR shielding tensors. *J. Chem. Phys.* **2009**, *131*, No. 101101.

(44) Sebastiani, D.; Parrinello, M. A New ab-Initio Approach for NMR Chemical Shifts in Periodic Systems. *J. Phys. Chem. A* **2001**, *105*, 1951−1958.

(45) Marsman, M.; Grüneis, A.; Paier, J.; Kresse, G. Second-Order Møller-Plesset Perturbation Theory Applied to Extended Systems. I. Within the Projector-Augmented-Wave Formalism Using a Plane Wave Basis Set. *J. Chem. Phys.* **2009**, *130*, No. 184103.

(46) Grüneis, A.; Marsman, M.; Kresse, G. Second-Order Møller-Plesset Perturbation Theory Applied to Extended Systems. Ii. Structural and Energetic Properties. *J. Chem. Phys.* **2010**, *133*, No. 074107.

(47) Schimka, L.; Harl, J.; Stroppa, A.; Grüneis, A.; Marsman, M.; Mittendorfer, F.; Kresse, G. Accurate Surface and Adsorption Energies from Many-Body Perturbation Theory. *Nat. Mater.* **2010**, *9*, 741−744.

(48) Grüneis, A.; Booth, G. H.; Marsman, M.; Spencer, J.; Alavi, A.; Kresse, G. Natural Orbitals for Wave Function Based Correlated Calculations Using a Plane Wave Basis Set. *J. Chem. Theory Comput.* **2011**, *7*, 2780.

(49) Booth, G.; Grüneis, A.; Kresse, G.; Alavi, A. Towards an Exact Description of Electronic Wavefunctions in Real Solids. *Nature* **2013**, *493*, 365.

(50) Usvyat, D.; Sadeghian, K.; Maschio, L.; Schütz, M. Geometrical Frustration of an Argon Monolayer Adsorbed on the Mgo (100) Surface: An Accurate Periodic Study. *Phys. Rev. B* **2012**, *86*, No. 045412.

(51) McClain, J.; Sun, Q.; Chan, G. K.-L.; Berkelbach, T. C. Gaussian-Based Coupled-Cluster Theory for the Ground-State and Band Structure of Solids. *J. Chem. Theory Comput.* **2017**, *13*, 1209−1218.

(52) Usvyat, D.; Maschio, L.; Schütz, M. Periodic and fragment models based on the local correlation approach. *WIREs: Comput. Mol. Sci.* **2018**, *8*, No. e1357.

(53) Boese, A. D.; Sauer, J. Accurate Adsorption Energies of Small Molecules on Oxide Surfaces: Co-Mgo(001). *Phys. Chem. Chem. Phys.* **2013**, *15*, 16481−16493.

(54) Stodt, D.; Noei, H.; Hattig, C.; Wang, Y. A Combined Experimental and Computational Study on the Adsorption and Reactions of NO on Rutile TiO2. *Phys. Chem. Chem. Phys.* **2013**, *15*, 466−472.

(55) Pöhlchen, M.; Staemmler, V. AbInitio Calculations for the Adsorption of Small Molecules on Metal Oxide Surfaces. I. Cluster Calculations for Carbon Monoxide CO on Nickel Oxide NiO(100). *J. Chem. Phys.* **1992**, *97*, 2583−2592.

(56) Libisch, F.; Huang, C.; Carter, E. A. Embedded Correlated Wavefunction Schemes: Theory and Applications. *Acc. Chem. Res.* **2014**, *47*, 2768.

(57) Kotliar, G.; Savrasov, S. Y.; Haule, K.; Oudovenko, V. S.; Parcollet, O.; Marianetti, C. A. Electronic Structure Calculations with Dynamical Mean-Field Theory. *Rev. Mod. Phys.* **2006**, *78*, No. 865.

(58) Sun, Q.; Chan, G. K. L. Quantum Embedding Theories. *Acc. Chem. Res.* **2016**, *49*, 2705.

(59) Olejniczak, M.; Bast, R.; Pereira Gomes, A. S. On the calculation of second-order magnetic properties using subsystem approaches in a relativistic framework. *Phys. Chem. Chem. Phys.* **2017**, *19*, 8400−8415.

(60) Jacob, C. R.; Visscher, L. Calculation of Nuclear Magnetic Resonance Shielding constants Using Frozen-Density Embedding. *J. Chem. Phys.* **2006**, *125*, No. 194104.

(61) Wesolowski, T. A.; Shedge, S.; Zhou, X. Frozen-Density Embedding Strategy for Multilevel Simulations of Electronic Structure. *Chem. Rev.* **2015**, *115*, 5891−5928.

(62) Hartman, J. D.; Balaji, A.; Beran, G. J. O. Improved Electrostatic Embedding for Fragment-Based Chemical Shift Calculations in Molecular Crystals. *J. Chem. Theory Comput.* **2017**, *13*, 6043−6051.

(63) Stanton, J. F.; Gauss, J.; Harding, M. E.; Szalay, P. G. et al. CFOUR, A Quantum Chemical Program Package. www.cfour.de. (accessed November, 2019).

(64) Jensen, F. Segmented Contracted Basis Sets Optimized for Nuclear Magnetic Shielding. *J. Chem. Theory Comput.* **2015**, *11*, 132.

(65) Neese, F. The Orca Program System. *WIREs: Comput. Mol. Sci.* **2012**, *2*, 73−78.

(66) Becke, A. D. Density-Functional Exchange-Energy Approximation with Correct Asymptotic-Behaviour. *Phys. Rev. A* **1988**, *38*, 3098−3100.

(67) Lee, C.; Yang, W.; Parr, R. G. LYP Functional. *Phys. Rev. B* **1988**, *37*, No. 785.

(68) Perdew, J. P.; Chevary, J. A.; Vosko, S. H.; Jackson, K. A.; Pederson, M. R.; Singh, D. J.; Fiolhais, C. Atoms, Molecules, Solids, and Surfaces: Applications of the Generalized Gradient Approximation for Exchange and Correlation. *Phys. Rev. B* **1992**, *46*, 6671−6687.

(69) Perdew, J. P.; Burke, K.; Ernzerhof, M. Generalized Gradient Approximation Made Simple. *Phys. Rev. Lett.* **1996**, *77*, No. 3865.

(70) Perdew, J. P. Density-Functional Approximation for the Correlation-Energy of the Inhomogeneous Electron-Gas. *Phys. Rev. B* **1986**, *33*, 8822−8824.

(71) Zhao, Y.; Truhlar, D. G. The M06 suite of density functionals for main group thermochemistry, thermochemical kinetics, noncovalent interactions, excited states, and transition elements: Two new functionals and systematic testing of four M06-class functionals and 12 other functionals. *Theor. Chem. Acc.* **2006**, *120*, 215−241.

(72) Becke, A. D. Density-Functional Thermochemistry. III. The Role of Exact Exchange. *J. Chem. Phys.* **1993**, *98*, No. 5648.

(73) Perdew, J. P.; Ernzerhof, M.; Burke, K. Rationale for Mixing Exact Exchange with Density Functional Approximations. *J. Chem. Phys.* **1996**, *105*, 9982−9985.

(74) Perdew, J. P.; Tao, J.; Staroverov, V. N.; Scuseria, G. E. Metageneralized Gradient Approximation: Explanation of a Realistic Nonempirical Density Functional. *J. Chem. Phys.* **2004**, *120*, 6898−6911.

(75) Tao, J.; Perdew, J. P.; Staroverov, V. N.; Scuseria, G. E. Climbing the Density Functional Ladder: Nonempirical Meta−Generalized Gradient Approximation Designed for Molecules and Solids. *Phys. Rev. Lett.* **2003**, *91*, No. 146401.

(76) Grimme, S. Semiempirical Hybrid Density Functional with Perturbative Second-Order Correlation. *J. Chem. Phys.* **2006**, *124*, No. 034108.

(77) Kozuch, S.; Martin, J. M. L. Spin-Component-Scaled Double Hybrids: An Extensive Search for the Best Fifth-Rung Functionals Blending DFT and Perturbation Theory. *J. Comput. Chem.* **2013**, *34*, 2327.

(78) Kozuch, S.; Martin, J. M. L. DSD-PBEP86: In Search of the Best Double-Hybrid Dft with Spin-Component Scaled MP2 and Dispersion Corrections. *Phys. Chem. Chem. Phys.* **2011**, *13*, 20104.

(79) Kozuch, S.; Gruzman, D.; Martin, J. M. L. DSD-BLYP: A General Purpose Double Hybrid Density Functional Including Spin Component Scaling and Dispersion Correction. *J. Chem. Phys. C* **2010**, *114*, 20801−20808.

(80) Eichkorn, K.; Treutler, O.; Öhm, H.; Häser, M.; Ahlrichs, R. Auxiliary Basis Sets to Approximate Coulomb Potentials. *Chem. Phys. Lett.* **1995**, *240*, 283−290.

(81) Neese, F.; Wennmohs, F.; Hansen, A.; Becker, U. Efficient, Approximate and Parallel Hartree−Fock and Hybrid DFT Calculations. A 'Chain-of-Spheres' Algorithm for the Hartree−Fock Exchange. *Chem. Phys.* **2009**, *356*, 98−109.

(82) Izsák, R.; Neese, F. An Overlap Fitted Chain of Spheres Exchange Method. *J. Chem. Phys.* **2011**, *135*, No. 144105.

(83) Weigend, F. Hartree-Fock Exchange Fitting Basis Sets for H to Rn. *J. Comput. Chem.* **2006**, *2*, 167−175.

(84) Weigend, F.; Häser, M.; Patzelt, H.; Ahlrichs, R. RI-MP2: optmized auxilary basis sets and demonstration of efficiency. *Chem. Phys. Lett.* **1998**, *294*, 143−152.

(85) Hättig, C. Optimization of auxiliary basis sets for RI-MP2 and RI-CC2 calculations: Core−valence and quintuple-f basis sets for H to Ar and QZVPP basis sets for Li to Kr. *Phys. Chem. Chem. Phys.* **2005**, *7*, 59−66.

(86) Furness, J. W.; Verbeke, J.; Tellgren, E. I.; Stopkowicz, S.; Ekström, U.; Helgaker, T.; Teale, A. M. Current Density Functional Theory Using Meta-Generalized Gradient Exchange-Correlation Functionals. *J. Chem. Theory Comput.* **2015**, *11*, 4169−4181.

(87) Tellgren, E. I. T.; Teale, A. M.; Furness, J. W.; Lange, K. K.; Ekström, U.; Helgaker, T. Non-perturbative calculation of molecular magnetic properties within current-density functional theory. *J. Chem. Phys.* **2014**, *140*, No. 034101.

(88) Lee, A. M.; Handy, N. C.; Colwell, S. M. The density functional calculation of nuclear shielding constants using London atomic orbitals. *J. Chem. Phys.* **1995**, *103*, 10095−10109.

(89) Malkin, V. G.; Malkina, O. L.; Casida, M. E.; Salahub, D. R. Nuclear Magnetic Resonance Shielding Tensors Calculated with a Sum-over-States Density Functional Perturbation Theory. *J. Am. Chem. Soc.* **1994**, *116*, 5898−5908.

(90) Reimann, S.; Ekström, U.; Stopkowicz, S.; Teale, A. M.; Borgoo, A.; Helgaker, T. The importance of current contributions to shielding constants in density-functional theory. *Phys. Chem. Chem. Phys.* **2015**, *17*, 18834−18842.

(91) Saue, T.; Bast, R.; Gomes, A. S. P.; Jensen, H. J. A.; Visscher, L.; Aucar, I. A.; Di Remigio, R.; Dyall, K. G.; Eliav, E.; Fasshauer, E.; Fleig, T.; Halbert, L.; Hedegård, E. D.; Helmich-Paris, B.; Iliaš, M.; Jacob, C. R.; Knecht, S.; Laerdahl, J. K.; Vidal, M. L.; Nayak, M. K.; Olejniczak, M.; Olsen, J. M. H.; Pernpointner, M.; Senjean, B.; Shee, A.; Sunaga, A.; van Stralen, J. N. P. The DIRAC code for relativistic molecular calculations. *J. Chem. Phys.* **2020**, *152*, No. 204104.

(92) Barysz, M.; Sadlej, A. J.; Snijders, J. G. Nonsingular two/one-component relativistic Hamiltonians accurate through arbitrary high order in $\alpha 2$. *Int. J. Quantum Chem.* **1997**, *65*, 225−239.

(93) Barysz, M.; Sadlej, A. J. Two-component methods of relativistic quantum chemistry: fromthe Douglas±Kroll approximation to the exact two-componentformalism. *J. Mol. Struct.: THEOCHEM* **2001**, *573*, 181−200.

(94) Barysz, M.; Sadlej, A. J. Infinite-order two-component theory for relativistic quantum chemistry. *J. Chem. Phys.* **2002**, *116*, 2696−2704.

(95) Iliaš, M.; Jensen, H. J. A.; Kello, V.; Roos, B. O.; Urban, M. Theoretical study of PbO and the PbO anion. *Chem. Phys. Lett* **2005**, *408*, 210−215.

(96) Dyall, K. G. Relativistic double-zeta, triple-zeta, and quadruple-zeta basis sets for the 4s, 5s, 6s, and 7s elements. *J. Phys. Chem. A* **2009**, *113*, 12638.

(97) Dyall, K. G. Core correlating basis functions for elements 31−118. *Theor. Chem. Acc.* **2012**, *131*, 1217.

(98) Dyall, K. G. An exact separation of the spin-free and spin-dependent terms of the Dirac−Coulomb−Breit Hamiltonian. *J. Chem. Phys.* **1994**, *100*, 2118−2127.

(99) Maldonado, A. F.; Aucar, G. A. Relativistic and Electron-Correlation Effects on the Nuclear Magnetic Resonance Shieldings of Molecules Containing Tin and Lead Atoms. *J. Phys. Chem. A* **2014**, *118*, 7863−7875.

(100) Downs, R. T.; Hall-Wallace, M. The American Mineralogist Crystal Structure Database. *Am. Mineral.* **2003**, *88*, 247−250.

(101) Gražulis, S.; Daškevič, A.; Merkys, A.; Chateigner, D.; Lutterotti, L.; Quirós, M.; Serebryanaya, N. R.; Moeck, P.; Downs, R. T.; Le Bail, A. Crystallography Open Database (Cod): An Open-Access Collection of Crystal Structures and Platform for World-Wide Collaboration. *Nucleic Acids Res.* **2012**, *40*, D420−D427.

(102) Gražulis, S.; Chateigner, D.; Downs, R. T.; Yokochi, A. F. T.; Quiros, M.; Lutterotti, L.; Manakova, E.; Butkus, J.; Moeck, P.; Le Bail, A. Crystallography Open Database - an Open-Access Collection of Crystal Structures. *J. Appl. Crystallogr.* **2009**, *42*, 726−729.

(103) van Wüllen, C. On the use of effective core potentials in the calculation of magnetic properties, such as magnetizabilites and magnetic shieldings. *J. Chem. Phys.* **2012**, *136*, No. 114110.

(104) Hayashi, S.; Hayamizu, K. Accurate determination of NMR chemical shifts in alkali halides and their correlation with structural factors. *Bull. Chem. Soc. Jpn.* **1990**, *63*, 913−919.

(105) Dupree, R.; Smith, M. E. Solid-state Magnesium-25 N.m.r. Spectroscopy. *J. Chem. Soc., Chem. Commun.* **1988**, 1483−1485.

(106) Pallister, P. P.; Moudrakovski, I. L.; Ripmeester, J. A. Mg-25 ultra-high field solid state NMRspectroscopy and first principles calculations of magnesium compounds. *Phys. Chem. Chem. Phys.* **2009**, *11*, 11487−11500.

(107) Bastow, T. J.; Stuart, S. N. NMR Study of the Zinc Chalcogenides (ZnX, X = O, S, Se, Te). *Phys. Status Solidi (b)* **1988**, *145*, 719−728.

(108) Dittmer, A.; Izsák, R.; Neese, F.; Maganas, D. Accurate Band Gap Predictions of Semiconductors in the Framework of the Similarity Transformed Equation of Motion Coupled Cluster Theory. *Inorg. Chem.* **2019**, *58*, 9303−9315.

(109) Fuentealba, P.; Preuss, H.; Stoll, H.; Von Szentpály, L. A proper account of core-polarization with pseudopotentials: single valence-electron alkali compounds. *Chem. Phys. Lett.* **1982**, *89*, 418−422.

(110) Fuentealba, P.; Szentpaly, L.; Preuss, H.; Stoll, H. Pseudopotential calculations for alkaline-earth atoms. *J. Phys. B: At., Mol. Opt. Phys.* **1985**, *18*, 1287−1296.

(111) Dolg, M.; Wedig, U.; Stoll, H.; Preuss, H. Energy-Adjusted Abinitio Pseudopotentials for the 1st-Row Transition-Elements. *J. Chem. Phys.* **1987**, *86*, 866−872.

(112) Bergner, A.; Dolg, M.; Küchle, W.; Stoll, H.; Preuß, H. Ab initio energy-adjusted pseudopotentials for elements of groups 13−17. *Mol. Phys.* **1993**, *80*, 1431−1441.

(113) Maganas, D.; Roemelt, M.; Havecker, M.; Trunschke, A.; Knop-Gericke, A.; Schlögl, R.; Neese, F. First Principles Calculations of the Structure and V L-Edge X-Ray Absorption Spectra of V2O5 Using Local Pair Natural Orbital Coupled Cluster Theory and Spin-Orbit Coupled Configuration Interaction Approaches. *Phys. Chem. Chem. Phys.* **2013**, *15*, 7260−7276.

(114) Cox, S. R.; Williams, D. E. Representation of the Molecular Electrostatic Potential by a Net Atomic Charge Model. *J. Comput. Chem.* **1981**, *2*, 304−323.

(115) Wiberg, K. B.; Rablen, P. R. Comparison of Atomic Charges Derived via Different Procedures. *J. Comput. Chem.* **1993**, *14*, 1504−1518.

(116) Kubas, A.; Berger, D.; Oberhofer, H.; Maganas, D.; Reuter, K.; Neese, F. Surface Adsorption Energetics Studied with "Gold Standard" Wave-Function-Based Ab Initio Methods: Small-Molecule Binding to TiO2(110). *J. Phys. Chem. Lett.* **2016**, *7*, 4207−4212.

(117) Roemelt, M.; Maganas, D.; DeBeer, S.; Neese, F. A combined DFT and restricted open-shell configuration interaction method including spin-orbit coupling: application to transition metal L-edge X-ray absorption spectroscopy. *J. Chem. Phys.* **2013**, *138*, No. 204101.

(118) Maganas, D.; Roemelt, M.; Weyhermuller, T.; Blume, R.; Havecker, M.; Knop-Gericke, A.; DeBeer, S.; Schlögl, R.; Neese, F. L-edge X-ray absorption study of mononuclear vanadium complexes and spectral predictions using a restricted open shell configuration interaction ansatz. *Phys. Chem. Chem. Phys.* **2014**, *16*, 264−276.

(119) Atanasov, M.; Aravena, D.; Suturina, E.; Bill, E.; Maganas, D.; Neese, F. First principles approach to the electronic structure, magnetic anisotropy and spin relaxation in mononuclear 3d-transition metal single molecule magnets. *Coord. Chem. Rev.* **2015**, *289−290*, 177−214.

(120) Kantorovich, L. *Quantum Theory of the Solid State: An Introduction*; Springer: Dordrecht, Netherlands, 2004.

(121) Dračínský, M.; Unzueta, P.; Beran, G. J. O. Improving the accuracy of solid-state nuclear magnetic resonance chemical shift prediction with a simple molecular correction. *Phys. Chem. Chem. Phys.* **2019**, *21*, 14992−15000.

(122) Olejniczak, M.; Bast, R.; Saue, T.; Pecul, M. A simple scheme for magnetic balance in four-component relativistic Kohn−Sham calculations of nuclear magnetic resonance shielding constants in a Gaussian basis. *J. Chem. Phys.* **2012**, *136*, No. 014108.

(123) Olejniczak, M.; Bast, R.; Saue, T.; Pecul, M. Erratum: "A simple scheme for magnetic balance in four-component relativistic Kohn−Sham calculations of nuclear magnetic resonance shielding constants in a Gaussian basis" [J. Chem. Phys. 136, 014108 (2012)]. *J. Chem. Phys.* **2012**, *136*, No. 239902.

(124) Kaupp, M.; Malkina, O. L.; Malkin, V. G. Interpretation of 13C NMR chemical shifts in halomethyl cations. On the importance of spin-orbit coupling and electron correlation. *Chem. Phys. Lett.* **1997**, *265*, 55−59.

(125) Kaupp, M.; Malkina, O. L.; Malkin, V. G.; Pyykkö, P. How Do Spin−Orbit-Induced Heavy-Atom Effects on NMR Chemical Shifts Function? Validation of a Simple Analogy to Spin−Spin Coupling by Density Functional Theory (DFT) Calculations on Some Iodo Compounds. *Chem. - Eur. J.* **1998**, *4*, 118−126.

(126) Kaupp, M. *Calculation of NMR and EPR Parameters*; Wiley-VCHVerlag GmbH & Co. KGaA: Weinheim, 2004.

(127) Autschbach, J. *High Resolution NMR Spectroscopy: Understanding Molecules and their Electronic Structures*; Elsevier: Oxford, 2013.

(128) Vícha, J.; Novotný, J.; Komorovsky, S.; Straka, M.; Kaupp, M.; Marek, R. Relativistic Heavy-Neighbor-Atom Effects on NMR Shifts: Concepts and Trends Across the Periodic Table. *Chem. Rev.* **2020**, *120*, 7065−7103.

(129) Gromov, O. I.; Kuzin, S. V.; Golubeva, E. N. Performance of DFT methods in the calculation of isotropic and dipolar contributions to 14N hyperfine coupling constants of nitroxide radicals. *J. Mol. Model.* **2019**, *25*, No. 93.

(130) Medvedev, M. G.; Bushmarinov, I. S.; Sun, J.; Perdew, J. P.; Lyssenk, K. A. Density functional theory is straying from the path toward the exact functional. *Science* **2017**, *355*, 49−52.

(131) Witwicki, M. Density functional theory and ab initio studies on hyperfinecoupling constants of phosphinyl radicals. *Int. J. Quantum Chem.* **2018**, *118*, No. e25779.